AD_____

Award Number: DAMD17-98-1-8349

TITLE: ETACT - An Innovative Approach to Scintimammography

PRINCIPAL INVESTIGATOR: Frederic H. Fahey, D.Sc.

CONTRACTING ORGANIZATION: Bowman Gray School of Medicine
Winston-Salem, North Carolina 27157

REPORT DATE: July 2002

TYPE OF REPORT: Final

PREPARED FOR: U.S. Army Medical Research and Materiel Command
Fort Detrick, Maryland 21702-5012

DISTRIBUTION STATEMENT: Approved for Public Release;
Distribution Unlimited

The views, opinions and/or findings contained in this report are those of the author(s) and should not be construed as an official Department of the Army position, policy or decision unless so designated by other documentation.

REPORT DOCUMENTATION PAGE

Form Approved
OMB No. 074-0188

1. AGENCY USE ONLY (Leave blank)	2. REPORT DATE	3. REPORT TYPE AND DATES COVERED
	July 2002	Final (1 Jul 98 - 30 Jun 02)

4. TITLE AND SUBTITLE
ETACT - An Innovative Approach to Scintimammography

5. FUNDING NUMBERS
DAMD17-98-1-8349

6. AUTHOR(S)

Frederic H. Fahey, D.Sc.

7. PERFORMING ORGANIZATION NAME(S) AND ADDRESS(ES)

Bowman Gray School of Medicine
Winston-Salem, North Carolina 27157

E-Mail: ffahey@wfubmc.edu

8. PERFORMING ORGANIZATION REPORT NUMBER

9. SPONSORING / MONITORING AGENCY NAME(S) AND ADDRESS(ES)

U.S. Army Medical Research and Materiel Command
Fort Detrick, Maryland 21702-5012

10. SPONSORING / MONITORING AGENCY REPORT NUMBER

11. SUPPLEMENTARY NOTES

12a. DISTRIBUTION / AVAILABILITY STATEMENT

Approved for Public Release; Distribution Unlimited

12b. DISTRIBUTION CODE

13. ABSTRACT *(Maximum 200 Words)*

This project investigates the use of a novel approach to scintimammography (SMM) known as emission tuned aperture computed tomography (ETACT). In ETACT, a series of projections of the radionuclide distribution in the breast are acquired with fiducial markers. These data are reconstructed into tomographic slices. The hypothesis of this project is that ETACT will increase the diagnostic accuracy of SMM, and can be applied in a simple and practical manner. We have developed simulation models and have used these tools to investigate aperture size, angular disparity, number of projections, and the effect of attenuation and scatter. Apertures of 3-4 mm were determined to be optimal for ETACT. Smaller angular disparity of the projections led to slightly improved contrast but lower axial resolution. Seven projections is a good compromise between image quality and clinical practicality. A phantom experiment demonstrated the enhanced performance of ETACT compared to SPECT and planar imaging. Monte Carlo studies confirmed the findings of our simpler simulations that excluded scatter and attenuation. Biorthogonal merging of two ETACT image sets leads to improved lesion visualization. A hybrid system using optical markers can lead to high quality reconstructions.

14. SUBJECT TERMS	15. NUMBER OF PAGES
breast cancer, scintimammography, tomography	103
	16. PRICE CODE

17. SECURITY CLASSIFICATION OF REPORT	18. SECURITY CLASSIFICATION OF THIS PAGE	19. SECURITY CLASSIFICATION OF ABSTRACT	20. LIMITATION OF ABSTRACT
Unclassified	Unclassified	Unclassified	Unlimited

Table of Contents

Introduction

This project investigated the use of a novel approach to scintimammography (SMM) known as emission tuned aperture computed tomography (ETACT). ETACT is based on the more general tuned aperture computed tomography (TACT®) method used in radiography. TACT has been successfully applied in dentistry and conventional mammography. In ETACT, fiducial markers are placed around the object being imaged. A series of projection images are acquired using a standard gamma camera with a pinhole (or other) collimator from any angle and at any distance, as long as all of the markers are within the field of view of all projections. The data are then reconstructed into a series of tomographic slices which can easily be done on a PC. Thus ETACT requires no expensive, dedicated hardware. The beauty of this approach is that, if successful, this method could be applied in practically every hospital in the US, almost immediately. The main hypothesis of this project is that the application of ETACT will significantly increase the diagnostic and prognostic accuracy of SMM, particularly for small, nonpalpable lesions, and that this innovative method can be applied in the clinic in a simple, flexible and practical manner. The specific aims of this research are as follows:

1. to develop and utilize a computer simulation model of ETACT to determine the optimal parameters for its application and to compare it to conventional SMM,
2. to utilize phantom data to further compare ETACT to conventional SMM, both planar and SPECT, and
3. to design a clinical ETACT prototype system that will then be used in a subsequent preliminary clinical investigation.

In this report, we will present the results of our simulation and phantom experiments, the development of an approach to merge orthogonal ETACT data sets, and the investigation of the use of optical rather than radioactive fiducial markers. We will then discuss our development of a protocol for the clinical implementation of ETACT as well as future directions for this research.

Body of the Report

I. ETACT

In ETACT, one or more fiducial markers are placed about the patient's breast. A series of projection images are acquired with a pinhole-collimated, gamma camera. We use pinhole collimation for three reasons. First, pinhole collimators are routinely available for most portable, gamma cameras, making this method a straightforward approach that can be applied in practically any hospital. Secondly, we can take advantage of the high resolution associated with pinhole collimation. For a typical pinhole collimator of length 30 cm and pinhole diameter of 4 mm as well as an intrinsic spatial resolution of the detector of 3.5 mm, the system spatial resolution is approximately 5 mm compared to that of planar and SPECT imaging with a high resolution collimator of approximately 7 mm and 10 mm, respectively. Special inserts can be made that would reduce the pinhole diameter further improving the resolution. Thirdly, the collimator sensitivity is inversely proportional to the square of the aperture-to-object distance whereas the sensitivity of a parallel-hole collimator does not vary with collimator-to-object distance, thus reducing the contribution to the image of activity in other organs such as the heart of the liver.

Consider the technique known as "tomosynthesis" (Grant 1972). In this case, the detector (e.g., the gamma camera crystal) is always oriented parallel to the tomographic plane of interest. Several projections are acquired such that all of the aperture (pinhole) locations are known, coplanar and parallel to the tomographic plane of interest. A series of tomographic planes can be reconstructed by appropriately shifting the projection data and adding them together. All reconstructed planes are parallel to the detector plane. Tomosynthesis has been shown to be a very simple and effective manner of generating tomographic data. However, it places many constraints on the acquired projection data and aperture locations for all of the projections must be known.

ETACT alleviates these geometric constraints by using the projected locations of a series of fiducial markers to obtain knowledge concerning each projection (Fahey 2002, Fahey 2001, Webber 1997). Consider the case where the detector is still coplanar and parallel to the tomographic plane of interest, but the actual location is not known. A fiducial marker whose

location relative to the object is fixed is also imaged within each projection. Consider a reference plane whose location is the same as the aperture-to-detector distance, but whose location is opposite the detector (see Figure 3, Fahey 2001. *NB*: This reference in included in the Appendix). If we overlay all of the projections and simply add them, we are reconstructing the reference plane. If we determine the centroid of the projected locations of the marker, shift all of the data such that projected location of the marker coincides with the centroid and add the data together, we would reconstruct the plane that contains the fiducial marker and is parallel to the detector plane. If the projections are shifted by half that amount and added, then the plane that is half way between the marker and the reference plane is reconstructed. In this manner, any arbitrary plane can be reconstructed.

In the present implementation of ETACT, 5 markers are used, four of which are coplanar and one of which is not. The rationale for this choice is presented by Hemler et al. (Hemler 2002. A reprint is included in the appendix). The four coplanar markers are used to transform all of the acquired projections such that they appear to all have been acquired with the aperture in a common plane. The fifth marker is then used as described above to shift and add the projections to reconstruct the series of tomographic slices. It also has been demonstrated that this approach with the five fiducial markers can be used to reconstruct the data even if the detector in each projection is not in the same plane. In summary, if we acquire a series of projection images using a set of 5 fiducial markers (4 coplanar and one out of plane), we can reconstruct the data into a series of tomographic slices, even if the location of neither the detector nor the aperture is known. It is also not necessary to have the detector in the same plane or at the same distance in each projection. Therefore, ETACT is a simple and flexible method of acquiring and processing tomographic data.

II. Development of ETACT Simulation Models

We developed a computerized, simulation model of the acquisition of ETACT data. The model currently allows you to define an arbitrary 3D object with a set of markers. The activity associated with each component can be defined. Once the detector configuration and the object are defined, the detector can be moved interactively about the object and simulated projections can be obtained. These data can be subsequently reconstructed with the standard, ETACT

software. The projections are then blurred and Poisson noise added that are consistent with the spatial resolution and sensitivity, respectively, of the aperture size chosen. We have used this simulation model to evaluate the effect of the aperture size, angular disparity and the number of projections on contrast and contrast-to-noise.

In order to evaluate the effect of photon attenuation and scatter on the above simulations, we utilized the MCNP Monte Carlo simulation code to model ETACT. MCNP has been shown to provide similar results to the EGS4 code. In these simulations, the breast was modeled as a 15 cm hemisphere and the tumor as a 7.5 mm sphere. The pinhole diameter was 6 mm. The acquisition geometry consisted of 25 cm pinhole-to-detector distance and a 15 cm pinhole-to-tumor distance, the same as in the ray-tracing simulations. In these simulations, three cases were considered: uncollided gamma rays (attenuation but no scatter), total attenuated (attenuation and scatter) and unattenuated. These were compared to evaluate the effects of photon attenuation and scatter. We have also modified an existing anthropomorphic computer phantom (the Zubal phantom) for the evaluation of breast imaging.

III. Evaluation of Aperture Size, Angular Disparity and Number of Projections through Simulation

We modeled the breast as a hemisphere with 15 cm diameter. The tumor was modeled as a sphere in the center of the breast. We considered 3 tumor sizes (5, 7.5 and 10 mm) and 2 target-to-nontarget (T/NT) ratios (5:1 and 10:1). Five markers (4 coplanar and one out-of-plane) were placed lateral to the breast. The detector was modeled as a gamma camera with a 50x50 cm filed-of-view. The aperture-to-detector distance was 25 cm. The aperture-to-object distance of approximately 15 cm was chosen such that the object, including the markers, took up the majority of the field of view. Using our projection simulator, we constructed 7 noiseless projections for each aperture size. We investigated 6 aperture diameters (1,2,3,4,5,6 mm) and 3 angular disparities between the projections: +/- 10, 15 and 20 degrees. Based on the calculated system spatial resolution of each pinhole, the projection data were blurred with a gaussian kernel. Based on the sensitivity of each pinhole size, Poisson noise was added to each pixel. These data were then reconstructed using the standard TACT reconstruction software.

To evaluate these data, the slice through the middle of the tumor was visually selected and a region of interest (ROI) was drawn about the tumor and the maximum pixel value (Max) in the ROI was determined. A similar sized and shaped ROI was placed lateral to the tumor to evaluate the background activity. The mean pixel value (BKG) and the standard deviation (SD_{BKG}) in the background ROI were determined. The contrast (C) was calculated using the formula

$$C = \frac{Max - BKG}{BKG}$$

A detectability index referred to as the contrast-to-noise ratio (CNR) was calculated by

$$CNR = \frac{C}{(SD_{BKG}/BKG)}$$

The results of this investigation are summarized in the Tables 2 and 3 of (Fahey 2001). As the aperture size is reduced, the contrast improves. This is expected due to the improved resolution and the subsequent reduction in the partial volume effect. However, the sensitivity decreases with reduced aperture size leading to fewer photons being acquired and thus a noisier image. Therefore, a 3 mm aperture is optimum with respect to the CNR although not substantially better than the 4 mm aperture.

The results of the angular disparity study are shown in Figures 2 and 3 as well as Table 1 of (Fahey 2002. This reference is included in the appendix). The contrast increases slightly with decreasing angular disparity. However, smaller angular disparity yields poorer axial spatial resolution. For example, no angular disparity yields a simple planar image without any axial resolution. From these results, a 15 degree angular disparity is determined to be a reasonable choice. Increasing the number of projections without increasing the total number of counts was shown to lead to an increase in contrast. If one knew the best, single projection to acquire, it may have higher contrast than ETACT, but one does not know the best projection, *a priori*. Thus, ETACT typically provides higher contrast than planar imaging. With more projections, there will be more set-up time extending the length of the study. Therefore, 6 or 7 projections are a reasonable number for the clinical implementation of ETACT.

IV. Monte Carlo Simulation Results

The results of the Monte Carlo simulation are shown in Figure 1 (see Appendix). This figure shows profiles of the counts through the tumor and breast for the three cases: uncollided, attenuated and no attenuation. The "no attenuation" case corresponds to the case used in the ray-tracing simulations. As shown in the figure, the three profiles are very similar except for the scale resulting from photon attenuation. The contrast for these cases is very similar. This study validates the conclusions drawn from the ray-tracing simulations.

V. Biorthogonal Imaging

All methods based on tomosynthesis yield poor resolution and streak artifacts in the direction orthogonal to the tomographic planes. We investigated whether combining the data from two orthogonal TACT data sets would minimize these artifacts (Webber 2001). This study was performed on transmission, mammographic data. A frozen autopsy breast sample was placed in a 35 mm cardboard box. Small lead markers ("Beekly spots") were placed on the corners of the box. The box was radiographed from 5 angles at angular disparities of -15, -7.5,0, 7.5 and 15 degrees. The box was then rotated 90 degrees and an analogous set of projections was acquired. The two data sets were reconstructed independently using the TACT algorithm and corrected for differential magnification between slices. The two 3D data sets were then combined via simple averaging of the pixel values. Projections through this merged data set were rendered either by linear averaging or by plotting the maximum value along each ray.

The results are illustrated in Figures 4 and 5 of (Webber 2001. *N.B.* This article is included in the Appendix). These figures show the linear and the maximum rendering, respectively. As can be seen, the individual image sets are well resolved in the direction normal to the reconstruction planes but resolution is substantially degraded in the orthogonal direction. However, the merged data set is well resolved at all angles. Although this experiment was performed with transmission data, the conclusions are applicable to ETACT as well. We plan to validate this in the next year.

VI. Use of Optical Fiducial Markers

The results from our simulation experiments indicate that we have to image at a substantial distance in order to include all of the fiducial markers in each projection. Imaging at such a distance leads to a substantial loss in the effectiveness of the pinhole collimator. The sensitivity and resolution of the pinhole collimator both degrade with increasing object-to-aperture distance. In addition, radioactive markers can be troublesome to make and can sometimes be mistaken for small tumors. For these reasons, we are investigating the use of optical fiducial markers. This is accomplished by mounting a digital camera on the gamma camera and acquiring both nuclear and optical images at each projection angle. The fiducial markers on the optical images are then used to reconstruct the radiologic image. After a thorough mathematical evaluation, we have determined that the optical image can be used *without* cross-calibration to the radiologic image, as long as the digital camera and the radiologic camera (e.g. gamma camera) are oriented such that they are both the same distance from the image plane and they are not rotated about the object in that plane. We have validated this approach through phantom experiments. (Webber 2002)

VII. Phantom Experiment and Comparison to Planar and SPECT SMM

We performed an experiment to compare the performance of ETACT to planar SMM and SPECT. We filled the various compartments of the Data Spectrum torso and breast phantom with the following activity concentrations:

Organ	Target Conc	Actual Conc
Torso (background)	0.3 μCi/mL	0.302 μCi/mL
Liver	0.6 μCi/mL	0.591 μCi/mL
Breast	0.3 μCi/mL	0.293 μCi/mL
Tumor (0.8 cm)	3.0 μCi/mL	2.5-2.9 μCi/mL

We based the target concentrations on what might be expected in a clinical setting. If 20 mCi is injected into a 60 kg patient and it distributes uniformly, then the activity concentration would be about 0.3 μCi/mL. We might expect the liver to possibly have twice that concentration. We targeted the tumor within the breast to have a target-to-nontarget ratio (T/NT) of 10:1. The

actual concentrations are based on the assayed amounts that were injected into each compartment. Due to the small amount of activity in the tumor, we expect that there is a range of the possible activity concentration in the tumor. This range corresponds to a T/NT in the range of 8.3-10.

For the ETACT acquisition, 6 projections were acquired over a 30 degree range using a 4 mm pinhole collimator. The distance between the pinhole aperture and the tumor was approximately 20 cm. Each image was acquired for 5 m (approximately 185 kcts per view). Six fiducial markers were placed about the breast to be used during the reconstruction: 4 coplanar markers were placed on the medial side of the breast, and the other 2 were placed on the lateral side on a line that was parallel to the plane containing the other 4. These data were reconstructed using the software developed by N. Linnenbrügger and R. Webber (TACTJ). A gaussian, smoothing filter (FWHM = 2 pixels) was applied to the reconstructed data to reduce the noise. Both the smoothed and unsmoothed data were analyzed.

The planar data were acquired in the lateral projection for 30 m (the same total time used to acquire the 6 ETACT projections). In this case, a low-energy, high-resolution parallel-hole collimator was used. At the image distances used, the number of counts acquired in the planar image exceeded that of the ETACT projections by about a factor of 2. Both the ETACT and the planar data were acquired on an ADAC TransCam portable gamma camera (30 cm field of view).

The SPECT acquisition was performed on an ADAC Forte, dual-head SPECT camera. We acquired the data for 124 total projections at 30 s per projection. Since this was a dual-headed camera, this acquisition took approximately 30 m. Thus all three modes of data acquisition took approximately the same amount of time. The SPECT data were reconstructed using filtered back-projection with a Hamming filter and a 0.6 cycles per Nyquist cut-off frequency.

We analyzed these data using the definitions contrast (C) and contrast-to-noise ratio (CNR) previously described. The results are listed below:

Method	Contrast	CNR	Comment
TACT	0.505	3.74	Tumor clearly seen
TACT (Smoothed)	0.266	7.89	Tumor clearly seen
Planar	0.260	3.94	Tumor barely seen
SPECT	0.022	0.92	Tumor not seen

These results indicate that the ETACT method provided improved detectability and visualization of the tumor that either the planar or SPECT methods. The tumor contrast was highest for the unsmoothed TACT image. Although the contrast in the planar image was lower, the substantially lower noise (due to the higher number of total counts) yielded a CNR value that was slightly higher than for ETACT. Smoothing the ETACT image greatly enhanced its CNR and also made the tumor more easily visible. Conversely, smoothing the planar data lead to a reduction in the CNR since the contrast was also substantially reduced. The tumor was not seen on the SPECT images as is indicated in the contrast and CNR values. This experiment confirms the simulation findings that ETACT has the potential for enhanced lesion detectability for small tumors in the breast.

VIII. Development of a Clinical Prototype

Based on these results, we have demonstrated the potential for ETACT to detect smaller tumors in the breast. We have also determined the following acquisition paramters for a clinical, ETACT protocol.

- 3-4 mm pinhole provides a good compromise between sensitivity and spatial resolution
- 6-7 projections provide a good ETACT reconstruction
- Total imaging time of 30 m (5 m per projection) provides adequate data
- 15^{o} angular disparity yields a good compromise between contrast and axial resolution
- 5 or 6 fiducial markers are adequate for reconstructed ETACT data
- Radioactive markers work adequately (must carefully choose μCi/mL)
- Use of optical markers needs further development

In addition, imaging the patient in the prone position with the breast suspended through a hole in the imaging table (or mattress) has been shown to be an effect way or acquiring the SMM study.

Based on these data and observations, the following protocol procedure is proposed.

1. The patient is injected with 20 mCi of ^{99m}Tc sestamibi.
2. The patient is placed in the prone position on the special SMM mattress with a hole cut out for the breast.
3. The breast to be imaged is suspended through the hole in the mattress with the nipple pointing down.
4. Four coplanar, radioactive, fiducial markers are placed on the medial side of the breast within the mattress hole. The 4 markers (~1 mCi/mL) form a square with sides of approximately 5 cm.
5. Two additional markers are placed on the lateral side of the breast on a line that is parallel to the plane containing the other 4 markers.
6. A pinhole collimator (3 or 4 mm aperture) is used with a portable or otherwise flexible gamma camera that will allow the acquisition of the ETACT projection images.
7. Six projections (5 m each) are acquired over a 30° arc that is centered on the straight lateral view of the breast.
8. The entire protocol should take less than 40 m per breast.

These projection data are then transferred to ETACT workstation and reconstructed suing the TACT algorithm. The resulting images can be reviewed as a stack of slices through the breast in conjunction with a three-dimensionally rendered reprojection of the data.

IX. Future Research Directions

With respect to using ETACT for SMM, several aspects of the data acquisition still deserve investigation. First, we will continue to investigate the use of optical markers to be used in the ETACT reconstruction. This approach would have the several advantages to the currently proposed method. We would not have to make radioactive markers. Care must be taken in making these such that they are "hot" enough to easily see, but not so hot as to obscure any clinically pertinent features. There is also a risk that the markers may leak. The use of optical markers may also allow the gamma camera to be placed closer to the area of interest. Currently, we must image at such a distance that all of the markers are always in the field of view. We may

be able to relax this requirement when using optical markers. Our mathematical treatment of this hybrid approach places several geometric constraints of the data acquisition. For instance, the pinhole aperture positions for all acquired projection must both be coplanar and parallel to the detector plane. The optical aperture positions for all projections must also be coplanar and this plane must also be parallel to the detector plane. We will investigate how closely we must adhere to these constraints in practical imaging situations.

We will investigate the use of other collimation besides pinhole with ETACT. For example, we will investigate the use of converging collimation that provides higher sensitivity at reasonable imaging distances than the pinhole while still providing better spatial resolution than parallel-hole collimation. An optimally designed converging collimator may allow for shorter imaging times and thus could be more easily applied in a clinical environment.

We would also like to investigate the application of ETACT with a more compact and flexible nuclear imaging camera. For example, the Digirad nuclear camera provides a 20x20 cm field of view that can be more easily brought into the mammography suite or into the operating room. If we can successfully apply ETACT with this or a camera with similar flexibility and portability, then we could potentially image the patient in the mammography suite while she is still in compression for her mammogram. In this manner, the ETACT imaging results could be correlated with the mammographic results to provide a combined approach that links the anatomical changes seen on mammography with the functional results seen with ETACT. With the currently proposed protocol, one of the limitations that still remains is that it is difficult to correlate the ETACT findings with those from mammography. The mammogram is used to direct the biopsy of any suspicious lesions. However, ETACT may provide a better indication of those aspects of the tumor that are metabolically active. Therefore, combining ETACT with mammography may improve the accuracy of stereotactic biopsy of the breast.

We will also look at applying ETACT to the imaging of the axillary lymph node region. Uptake of ^{99m}Tc sestamibi in this region can be indicative of the spread of the disease to the lymph system and thus may lead to a difference in the patient's prognosis. ETACT may provide a means for providing improved detection and localization of activity in the axilla. Such information may lead to more accurate staging of patients with breast cancer.

Beyond breast imaging, we are looking at the use of ETACT for small animal imaging. We can use pinhole collimation with a very small aperture (e.g., 1 mm) to image mice that have

been administered a radiopharmaceutical. ETACT provides an easy and straightforward manner of providing tomographic images of these animals. The 3D information provided by ETACT will provide an improved ability to quantify the amount of activity in the feature. Thus ETACT could not only be used to provide a means for testing new radiotracers in rodents, but could also be used for providing a better way of monitoring the success of new treatment regimens in rodent models using standard radiopharmaceuticals.

In this project we have shown that ETACT provides a simple and flexible manner of providing tomographic data from a series of projection images. This allows radionuclide tomography to be applied in a variety of imaging settings and applications which would be difficult for conventional tomographic approaches such as SPECT. For these reasons, we will continue to investigate the use of ETACT for both breast imaging as well as other applications and we suspect that other investigators will also start to look at this simple and flexible approach. Lastly, we thank the Department of Defense for their generous support during this project, and we look forward to working with them in the future.

IX. Review of Statement of Work

In this section, we will review the original statement of work with respect to work performed during this project.

Task 1: To develop and utilize a computer simulation model (Months 1-15) [*This has been completed.*]

- Develop female, thoracic computer phantom including breasts, tumor, lymph nodes, heart, liver and lungs [*This has been completed.*]
- Model radiologic properties of phantom including emission, detection, attenuation, scatter and Poisson noise [*This has been completed*]
- Model ETACT with number of fiducial markers, placement of markers, number and orientation of ETACT views [*This has been completed*]
- Model conventional SMM including both planar and SPECT [*This has been completed*]
- Run simulations varying lesion size, location and T/NT ratio [*This has been completed.*]
- Determine SNR and perform ROC analysis to compare different ETACT configurations to each other and to conventional SMM [*This has been completed.*]

Task 2: To acquire and utilize phantom data to further compare ETACT to conventional SMM [*This has been completed*]

- Develop phantom protocol including lesion placement, size and T/NT ratio and activity in other organs (heart, liver and chest) [*This has been completed*]
- Acquire ETACT data with portable gamma camera and pinhole collimator varying number and location of fiducial markers, number and location of views and reconstruction method [*This has been completed*]
- Acquire conventional SMM including planar and SPECT [*This has been completed*]
- Perform ROI analysis to determine the SNR in the phantom data [*This has been completed*]
- Perform ROC analysis to compare different implementations of ETACT to each other and to conventional SMM [*A modified version of this task has been completed.*]

Task 3: To design a clinical ETACT scintimammographic system prototype [*This has been completed*]

- Based on results of Tasks 1 and 2, design the optimal, acquisition parameters for ETACT SMM [*This has been completed*]
- Design a system for reliable and practical method of marker placement [*This has been completed*]
- Review design with both technical and physician staff in both nuclear medicine and mammography [*This has been completed*]
- Modify and finalize design based on clinical feedback. [*This has been completed*]

Key Research Accomplishments

Task 1: To develop and utilize a computer simulation model

- We have developed a 3D tool for simulating the ETACT acquisition process including emission, pinhole collimation, detection and Poisson noise.
- We have developed a simple breast tumor model for the evaluation of scintimammography.
- We have converted this application from SGI to NT to make it more accessible.
- We have performed an evaluation of the aperture size, angular disparity and number of projections using the simulation application described above.
- We have developed a Monte Carlo model of ETACT and used it to evaluate the effect of photon attenuation and scatter on ETACT.

Task 2: To acquire and utilize phantom data to further compare ETACT to conventional SMM

- We have acquired the Data Spectrum breast phantom and have developed a protocol for imaging this phantom with fiducial markers using a portable gamma camera with a pinhole collimator.
- We have performed a comparison between ETACT and SMM (both planar and SPECT) using phantom data.
- We have validated our simulation results and shown ETACT to be a clinically practical approach.

Task 3: To design a clinical ETACT scintimammographic system prototype

- We have developed a method of merging two orthogonal ETACT data sets to further improve image quality and tumor detectability.
- We are developing a method for using optical fiducial markers can be applied to ETACT in a practical manner.
- Based on the results of these studies and discussions with our clinical colleagues, we have developed a protocol for the clinical application of ETACT.

Reportable Outcomes

Fahey FH, Webber RL, Harkness BA. ETACT: a novel approach to scintimammography. J Nucl Med 1998; 39:24P (abstract, presented at the Society of Nuclear Medicine Annual Meeting, Toronto, June 1998)

Fahey FH, Webber RL, Bayram E, Harkness BA, Mu Z, Hemler P. Preliminary evaluation of ETACT scintimammography. Med Phys 1999; 26:1072 (abstract, presented at the American Association of Physicists in Medicine Annual Meeting, Nashville, July 1999)

Hemler PF, Webber RL, Fahey FH. Modeling and error identification of three dimensional tomosynthesis reconstructions. SPIE Proceedings. 2000;3979:1280-1287 (presented at the SPIE Symposium on Medical Imaging, February 2000)

Fahey FH, Grow KL, Webber RL, Bayram E, Harkness BA, Hemler PF. ETACT: A Novel Approach to Scintimammography. ERA of Hope Proceedings, Vol 1. 2000. (abstract, presented at the Era of Hope Meeting, Atlanta, June 2000)

Grow KL. Evaluation of emission tuned aperture computed tomography. Masters Thesis. Wake Forest University, 2000.

Fahey FH, Grow KL, Webber RL, Harkness BA, Bayram E, Hemler PF. Emission tuned-aperture computed tomography: a novel approach to scintimammography. J Nucl Med 2001;42:1121-1127.

Webber RL, Fahey FH. Biorthogonal merging of mammographic slices using tuned-aperture computed tomography. J Elect Imag. 2001; In Press.

Fahey FH, Grow KL, Meltsner MA, Webber RL. Angular disparity in ETACT scintimammography (abstract, accepted for presentation at Radiologic Society of North America, Chicago, November 2001).

Fahey FH, Rhyasen KL, Harkness BA, Meltsner MA, Webber RL. Angular disparity in ETACT scintimammography . Med Phys. 2002;29:1980-1983.

Webber RL, Robinson SB, Fahey FH. Three-dimensional, tuned-aperture computed tomography reconstruction using hybrid imaging systems. 2002; In Preparation.

Hemler PF, Robinson SB Webber RL, Fahey FH. Tuned-aperture computed tomography. 2002; Submitted to Med Phys.

The TACT simulation tool developed by Dr. Hemler (Hemler 2000) was supported in part by this project.

Masters degree in Physics obtained by Kerry L. (Grow) Rhyasen. Wake Forest Universitiy, 2000. Ms. Rhyasen was supported by this grant for 15 months. Based on the training she attained during this project, she is now a junior medical physicist at Stanford University.

Personnel receiving support via this grant

Frederic H. Fahey, D.Sc.
Richard L. Webber, Ph.D.
Paul F. Hemler, Ph.D.
Beth A. Harkness, M.S.
Kerry L. (Grow) Rhyasen, M.S.

Conclusions

We have implemented the ETACT reconstruction algorithm that we described in our application. We have further developed a computerized simulation model for the acquisition process associated with ETACT including emission, collimation, detection and Poisson noise. We have also developed a simple model for the breast with a small tumor which also includes the fiducial markers necessary for doing ETACT. We used these simulation tools to perform an evaluation of the aperture size, angular disparity and number of projections. Based on this evaluation, it was determined that a 3-4 mm diameter aperture was optimal for ETACT. We also developed a Monte Carlo model of ETACT that included attenuation and scatter to demonstrate the validity of our ray-tracing simulation results. Using this phantom, we performed an evaluation to test the validity of our simulations and the feasibility of this approach. We used the phantom experiment to compare ETACT to conventional SMM, both planar and SPECT. We found ETACT to provide high contrast images that could be used to detect and visualize small features that were not readily visible on either planar or SPECT images. These evaluations indicated that we need to greatly reduce the aperture-to-object distance if we are to improve the performance of ETACT. We demonstrated that merging 2 orthogonal ETACT data sets greatly improve image quality and tumor detectability. We implemented and tested an approach for using optical rather than radioactive markers. Based on the results of this project along with discussions with our clinical colleagues, we have developed a protocol for the clinical implementation of ETACT.

References

Fahey FH, Grow KL, Webber RL, Harkness BA, Bayram E, Hemler PF. Emission tuned-aperture computed tomography: a novel approach to scintimammography. J Nucl Med 2001;42:1121-1127.

Grant DG, Tomosynthesis: A three-dimensional radiographic imaging technique. IEEE Trans Biomed Engin 1972; BME-19:20-28.

Webber RL, Horton RA, Tyndall DA, Ludlow JB. Tuned-aperture computed tomography (TACT™). Theory and application for three-dimensional dento-alveolar imaging. Dentomaxill Radiol 1997; 26:53-62.

Webber RL, Fahey FH. Biorthogonal merging of mammographic slices using tuned-aperture computed tomography. J Elect Imag. 2001; In Press.

Fahey FH, Rhyasen KL, Harkness BA, Meltsner MA, Webber RL. Angular disparity in ETACT scintimammography . Med Phys. 2002;29:1980-1983.

Webber RL, Robinson SB, Fahey FH. Three-dimensional, tuned-aperture computed tomography reconstruction using hybrid imaging systems. 2002; In Preparation.

Hemler PF, Robinson SB Webber RL, Fahey FH. Tuned-aperture computed tomography. 2002; Submitted to Med Phys.

Appendix

This appendix includes the Figure 1 from the *Body of the Report* and

Fahey FH, Grow KL, Webber RL, Harkness BA, Bayram E, Hemler PF. Emission tuned-aperture computed tomography: a novel approach to scintimammography. J Nucl Med 2001;42:1121-1127.

Webber RL, Fahey FH. Biorthogonal merging of mammographic slices using tuned-aperture computed tomography. J Elect Imag. 2001; In Press.

Fahey FH, Rhyasen KL, Harkness BA, Meltsner MA, Webber RL. Angular disparity in ETACT scintimammography . Med Phys. 2002;29:1980-1983.

Webber RL, Robinson SB, Fahey FH. Three-dimensional, tuned-aperture computed tomography reconstruction using hybrid imaging systems. 2002; In Preparation.

Hemler PF, Robinson SB Webber RL, Fahey FH. Tuned-aperture computed tomography. 2002; Submitted to Med Phys.

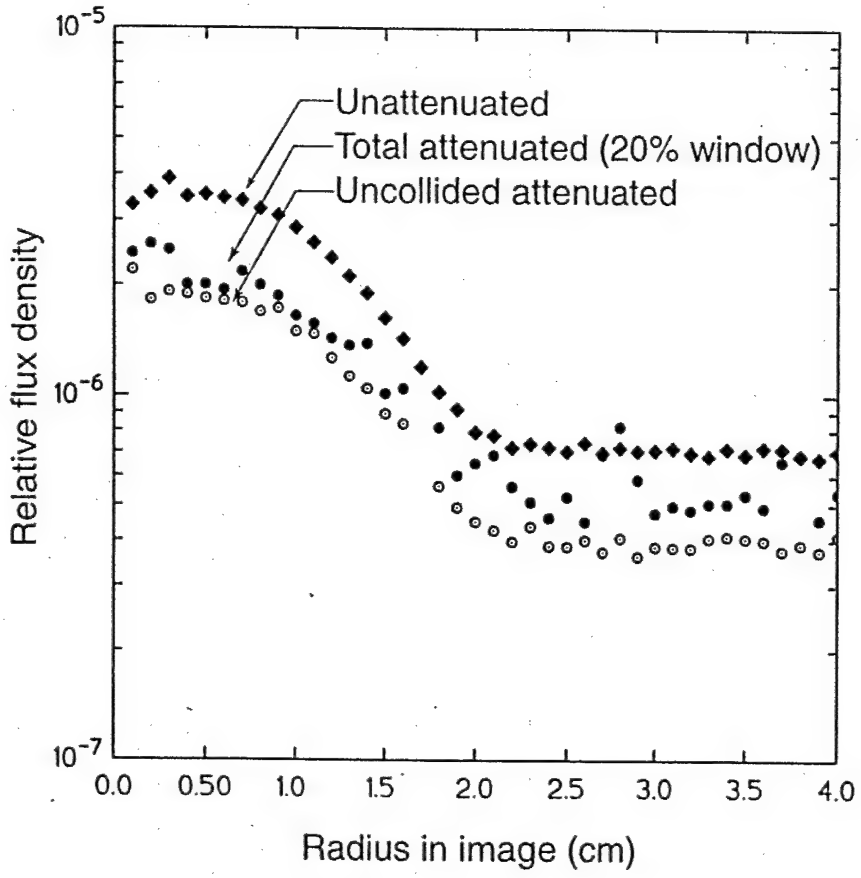
10^{-5}
10^{-6}
10^{-7}
Relative flux density
Unattenuated
Total attenuated (20% window)
Uncollided attenuated
0.0
0.50
1.0
1.5
2.0
2.5
3.0
3.5
4.0
Radius in image (cm)

Figure 1

Emission Tuned-Aperture Computed Tomography: A Novel Approach to Scintimammography

Frederic H. Fahey, Kerry L. Grow, Richard L. Webber, Beth A. Harkness, Ersin Bayram, and Paul F. Hemler

Division of Radiologic Sciences, Wake Forest University School of Medicine, and Department of Physics, Wake Forest University, Winston-Salem, North Carolina

Emission tuned-aperture computed tomography (ETACT) is a new approach to acquiring and processing scintimammography data. A gamma camera with a pinhole collimator is used to acquire projections of the radionuclide distribution within the breast. Fiducial markers are used to reconstruct these projections into tomographic slices. Simulation and phantom experiments were performed to evaluate the potential of the ETACT method. **Methods:** In the simulation study, a hemispheric object of 15 cm in diameter was constructed to model a breast. A ray-tracing technique was used to generate ideal projections. These were blurred and noise was added to create images that resemble scintigraphic images. Tumor size, pinhole size, and target-to-nontarget radioactivity ratios (TNTs) were varied. The simulated projections were reconstructed into slices, and contrast and contrast-to-noise ratios were calculated to evaluate the effect of pinhole size. These results were compared with a simulated planar acquisition of the same object. A preliminary phantom evaluation was performed using an 8-mm "tumor" with a 10:1 TNT to validate the simulation results. **Results:** A 3-mm pinhole was shown by the simulation study to be the optimal size. The ETACT images consistently yielded higher contrast than simulated planar images. The phantom study validated the simulation results and showed the feasibility of ETACT in a simulated clinical environment. **Conclusion:** ETACT is shown to be useful for imaging tumors <1 cm in diameter. Because ETACT requires only a gamma camera with a pinhole collimator, it has the potential to be applied in any hospital in a simple, flexible, and practical manner.

Key Words: tomography; pinhole collimation; reconstruction

J Nucl Med 2001; 42:1121–1127

Breast cancer is the most common malignancy among women in the United States (*1*). Every year, more than 185,000 lives are impacted as a result of breast cancer and 44,000 die of the disease (*2*). Patients with breast cancer diagnosed at a localized stage experience a survival rate of 90%, whereas the rate is <20% if the cancer has spread to 1 or more distant sites (*3*). Early detection, therefore, plays an essential role in the fight against breast cancer. Although mammography is currently the best imaging approach for breast cancer screening, several factors may limit its accuracy. Dense breasts, breast implants, or scars may either resemble a tumor or hide true small tumors on the mammogram. As a result, false-positive as well as false-negative incidents are increased. Mammography has a relatively high sensitivity (88%), although dense or large breasts may reduce this. However, it has a low specificity (67%) (*4*).

Scintimammography using ^{99m}Tc-labeled sestamibi has been shown to have high sensitivity and specificity (93.7% and 87.8%, respectively) for tumors >1.5 cm (*5*). However, in its current implementation, the limited spatial resolution of the gamma camera limits the sensitivity and specificity for tumors <1 cm (*6*). We are developing a new approach to detect early stages of breast cancer with scintimammography called emission tuned-aperture computed tomography (ETACT). ETACT uses pinhole collimation and limited angle tomography to potentially improve the contrast of small tumors. In this article, we describe the ETACT method and present some preliminary simulation and phantom investigations of this approach.

ETACT is based on the tuned-aperture computed tomography (TACT) method developed by Webber et al. (*7*). Consider the tomographic method known as tomosynthesis (*8*). In tomosynthesis, several planes through an object are reconstructed from a small number of 2-dimensional (2D) projections. This technique is illustrated in Figure 1. A series of coplanar x-ray sources form a circular pattern. A disk and a square are located between the source and detector planes. Each source projects the 2 objects onto the detector plane, resulting in a series of projections. By shifting by the appropriate amount and then adding these projections, any plane through the object can be reconstructed. For instance, if all projections are shifted so that the centers of the disk in all images are aligned and the projections are then added together, the result is the slice that contains the disk being reconstructed. Note that the square object is out of focus in this plane. However, by shifting such that the squares align and then adding, the plane through the square

Received Nov. 2, 2000; revision accepted Mar. 8, 2001.

For correspondence or reprints contact: Frederic H. Fahey, DSc, PET Center, Wake Forest University School of Medicine, Medical Center Blvd., Winston-Salem, NC 27157-1061.

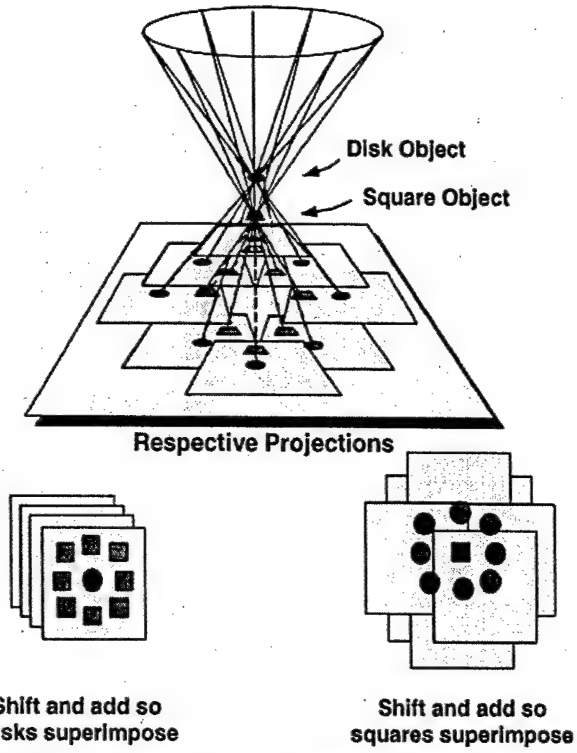

FIGURE 1. Tomosynthesis is imaging technique that shifts and adds series of 2D projections to construct 3-dimensional image. Point sources of each projection are coplanar, leading to linear shifting and adding of projections. Through shifting and adding process, any arbitrary slice through object can be reconstructed. (Reprinted with permission of (*7*).)

can also be reconstructed. In this fashion, any slice through the object can be created, and a 3-dimensional (3D) representation of the object is constructed. In tomosynthesis, the amount to shift the projections before addition is determined from the known location of the x-ray sources.

In TACT, the imaging geometry is more flexible and the source is not restricted to 1 plane. This allows more freedom to "tune" the projections to each situation, thus optimizing the reconstruction. As a result of this loosened geometry, fiducial markers are needed to compensate for the extra degrees of freedom. First, consider the sources to be located in a plane parallel to the detector plane, but with unknown position within that plane, as shown in Figure 2. A single fiducial marker is used. If all projections are added without shifting, we are reconstructing the detector plane. The centroid of the fiducial marker locations in all projections is then calculated. The projections are shifted such that the locations of the fiducial marker in the different projections align with the centroid and are then added together. The result is the reconstruction of the slice containing the fiducial marker as shown in Figure 2. To reconstruct a slice one third of the way between the marker and the detector plane, the projections are shifted two thirds the distance between their initial location and the centroid and added together. In this fashion any arbitrary slice can be reconstructed and a 3D representation of the object is constructed (*7*).

Now consider a situation in which the source locations are not coplanar and their locations are unknown. In this case, at least 5 fiducial markers (e.g., 4 coplanar and 1 out of plane) are needed. The 4 coplanar markers are used to apply a projective transformation between the projections and a reference image. This provides a correction for skewing and a first-order correction for magnification. The magnification correction applies only to the plane containing the 4 fiducial markers and does not correct for the differential magnification between planes. Once this transformation has been applied to the projections, they can be treated as if they were acquired with coplanar sources and the fifth, out-of-plane fiducial marker is used to reconstruct the data as described previously (i.e., shifting and adding). TACT has been used successfully in a variety of radiographic applications including dental radiography and mammography (*7,9*).

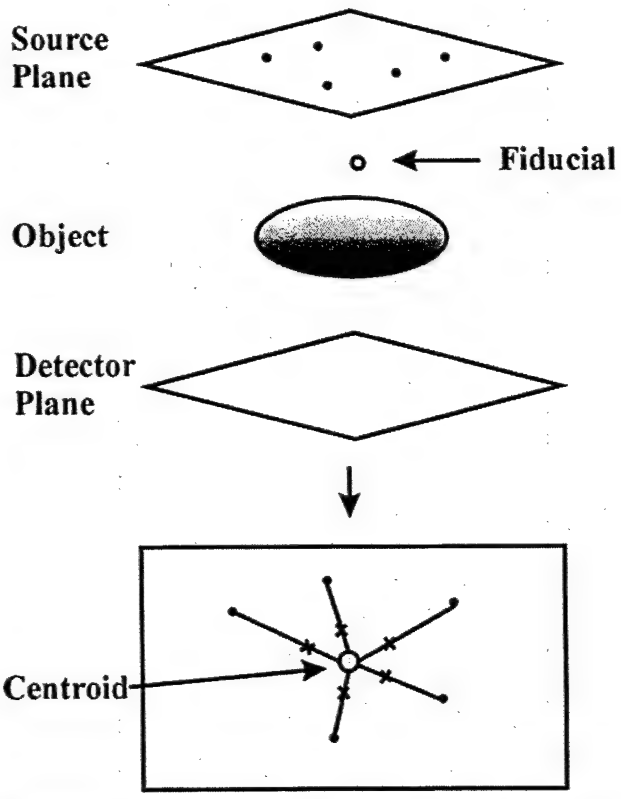

FIGURE 2. Demonstration of concepts of TACT. Five x-ray source locations are coplanar but arbitrary and unknown. One fiducial marker is used. Five projections of object are obtained. If projections are added without shifting, object at detector plane is reconstructed. Centroid of 5 marker locations is determined. If all projections are shifted such that marker locations align with centroid and projections are then added, plane containing fiducial marker is reconstructed. To reconstruct plane one third of way from marker to detector plane, projections are shifted two thirds of distance from their initial location toward centroid and then added. In this manner, any arbitrary plane can be reconstructed and 3D representation of object is obtained.

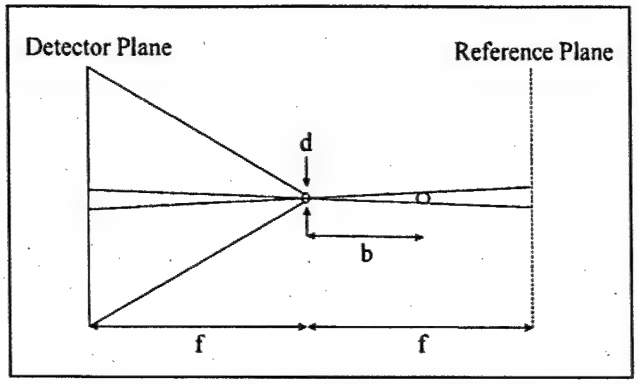

FIGURE 3. Similarity between TACT and ETACT geometry, where d is pinhole diameter, b is pinhole-to-object distance, and f is distance from pinhole to both detector and reference planes. In ETACT, reference plane is parallel to detector plane and same distance from pinhole, but on opposite side of pinhole. In ETACT, pinhole is analogous to source in TACT.

ETACT is emission TACT, which combines the concept of TACT with nuclear medicine imaging. A radiopharmaceutical is injected into the patient and imaged with a gamma camera using a pinhole collimator. In this geometry, the x-ray source in TACT is replaced with the pinhole collimator. The detector plane is the surface of the NaI detector. A reference plane is defined that is parallel to the detector plane and equidistant to the pinhole but on the opposite side, as shown in Figure 3. The pinhole location is not restricted to 1 plane. This allows the freedom to choose projection angles, which will be optimized for each specific imaging situation. The 5 fiducial markers are radioactive in ETACT. After the projective transformation of the projections (using the 4 coplanar markers), adding the projections without shifting reconstructs the reference plane. Shifting all projections so that the fifth fiducial marker locations in all images align with their centroid reconstructs the plane parallel to the reference plane and containing the fifth marker. Shifting the projections a set fraction of that amount reconstructs the plane that is that fraction of the distance between the fifth fiducial marker and the reference plane. Therefore, ETACT can reconstruct any number of slices and thereby generate a 3D representation of the object.

Potential benefits of ETACT arise from both the use of pinhole collimation and the flexibility of the ETACT acquisition. In the first case, the pinhole collimator provides superior spatial resolution to that of a parallel-hole collimator. For a pinhole-to-detector distance of 25 cm, a pinhole diameter of 4 mm, and an intrinsic spatial resolution of 3.5 mm, the pinhole system spatial resolution is approximately 6.0 mm compared with that of planar and SPECT imaging with a high-resolution collimator, which would be approximately 7.5 and 10 mm, respectively. This increased spatial resolution will lead to enhanced contrast of small tumors attributed to a reduction in the partial-volume effect. Second, the sensitivity of the pinhole collimator is inversely proportional to the square of the pinhole-to-object distance, whereas the sensitivity of a parallel-hole collimator does not vary with distance. Therefore, the pinhole collimator will be less sensitive to activity in objects behind the breast such as the myocardium or the liver. For example, if we assume that radioactivity in the tumor and myocardium is located 7 and 14 cm from the pinhole, respectively, then the system will be 4 times more sensitive to activity in the tumor than it is to the myocardium.

The advantage of ETACT over other tomographic methods is that the 3D resolution as well as the signal to noise can be "tuned" to specific diagnostic tasks through purposeful manipulation of the data-sampling strategy. This is analogous to altering one's vantage point to optimize the viewing of a scene or manipulating the optical aperture of a camera to adjust the depth of focus to best fit the imaging task at hand. Therefore, the projections obtained during an ETACT acquisition can be chosen to avoid signals from other organs such as the heart or liver or to enhance the tomographic capability for challenging imaging tasks such as the detection of small tumors near the chest wall.

On the basis of both of these factors, ETACT has the potential to enhance the detection of small tumors in the breast. Pinhole collimation enhances system spatial resolution and degrades the contribution of signal from other organs, and TACT reconstruction further enhances the contrast of these small structures. The result should be an overall increase in the signal-to-noise ratio (SNR) and, thereby, detectability for small tumors. Clinically, this should result in improvements in sensitivity and specificity for the detection of breast tumors <1 cm in diameter.

MATERIALS AND METHODS

Simulation Experiments

Simulation studies were used to determine the optimal pinhole size for ETACT. An object was designed whose shape resembled that of a hemispheric breast, 15 cm in diameter. A spheric tumor was placed in the center of the breast. The tumor was assigned a diameter of 5, 7.5, or 10 mm. Five fiducial markers were placed to the lateral side of the breast. Four of the markers were coplanar (parallel to a sagittal plane through the breast) and formed a square, 5×5 cm, whereas the fifth fiducial marker was out of the plane by 1 cm. The target-to-nontarget radioactivity ratio (TNT) was also defined. In various simulations the TNT was 5:1 (i.e., the tumor was 5 times as "hot" as the rest of the breast), 7.5:1, 10:1, 12.5:1, or 15:1. The 3D object was represented as a series of 40 equally spaced slices. Projections of this object were generated using a ray-tracing technique (*10*). The detector was defined as a 500×500 mm square to ensure that all projections would be within the field of view. The pinhole-to-detector and pinhole-to-object (tumor) distances were 25 and 15 cm, respectively. A symmetric set of angles was used to take 7 projections of the object. The first image was a straight lateral view of the breast. From the straight lateral, let the angle θ describe the amount of caudal tilt and the angle ϕ describe the amount of rotation about the long axis of the body. The other 6 projections were acquired in a hexagonal pattern with each view 15° from the straight lateral as described in Table 1. Note that $\theta = 10°$ and $\phi = 10°$ lead to an angle from the straight lateral of about 15°. These 7 projections

TABLE 1
Angular Orientation of Each Simulated Projection

Projection	Angle (°)	
	θ	ϕ
1	0	0
2	15	0
3	−15	0
4	10	10
5	−10	10
6	10	−10
7	−10	−10

From straight lateral, let angle θ describe amount of caudal tilt and angle ϕ describe amount of rotation about long axis of body. Note that θ = 10° and ϕ = 10° lead to angle from straight lateral of about 15°.

were considered "ideal," meaning no blurring or noise was added. These projections were then blurred and noise was added, depending on the pinhole size, which was varied: 1, 2, 3, 4, 5, and 6 mm in diameter. The blurring was accomplished by convolving the projections with a gaussian kernel having SD σ with:

$$\sigma = R_{sys}/2.35,$$

$$\text{with } R_{sys} = (R_{ph}^2 + (R_I/M)^2)^{1/2},$$

$$R_{ph} = \frac{d}{f}(f + b),$$

$$\text{and } M = \frac{f}{b},$$

where d is the pinhole diameter, f is the pinhole-to-detector distance, b is the pinhole-to-object distance, M is the magnification factor, R_I is the intrinsic resolution, R_{sys} is the system resolution, and R_{ph} is the pinhole resolution (*11*).

Noise was then added to each projection. First, the projection data were scaled such that the pixel values were similar to that acquired with a gamma camera using a pinhole collimator. The sensitivity was calculated on the basis of the pinhole size, using (*11*):

$$G = \frac{1}{16}(d/f)^2(b + f).$$

The scaled projection was multiplied by the sensitivity on a pixel-by-pixel basis. Each pixel value was sampled from a Poisson distribution with a mean N, where N is the noiseless pixel value. Projection sets were generated for various tumor sizes, TNTs, and pinhole sizes. All sets were simulated twice, once using blurred data and once using data that were both blurred and noisy. A total of 36 ideal projection sets was simulated.

For each projection set, the TACT software developed by R.A. Horton and R.L. Webber (Verity Software Systems, Winston-Salem, NC) was used to reconstruct the data. The straight lateral view was used as the reference. The 4 coplanar fiducial markers were identified on each projection, and a projective transformation of each of the projection images was performed. The fifth marker was identified in each projection and used to determine the amount of shifting necessary to reconstruct different slices through the object. Figure 4 displays 4 of 40 reconstructed slices of the blurred and noisy case for the 10-mm tumor and 10:1 TNT and a 3-mm pinhole. Because the lateral view was used in each case as the reference image, all reconstructed image sets were oriented in the same way. For each case, the slice with the tumor was selected. Contrast measurements of tumor counts versus background counts in the blurred image were calculated and recorded. A 16 × 16 pixel region of interest (ROI) was used to determine the counts over the tumor. A similarly sized ROI was placed in the background of the breast, just outside of the tumor boundary. Two measurements were made in the background and then averaged. One measurement was made directly on the tumor and the value (TUM) was recorded. The contrast was then estimated using the following formula:

$$C = \frac{(TUM - BKG)}{BKG},$$

where BKG is the mean value of the pixel counts in a background ROI. The fractional SD (FSD = SD/BKG) of the pixel values in the background of the blurred and noisy image was also calculated. Two FSD measurements were taken from the background of the breast and then averaged together. The contrast, C, was divided by the averaged FSD to estimate the contrast-to-noise ratio (CNR):

$$CNR = \frac{C}{FSD}.$$

The CNR is analogous to the SNR. Calculation of the SNR would require the fractional SD of the ROI counts rather than the pixel counts. However, if the pixel counts in the region are reasonably uniform, the 2 SDs should be proportional to each

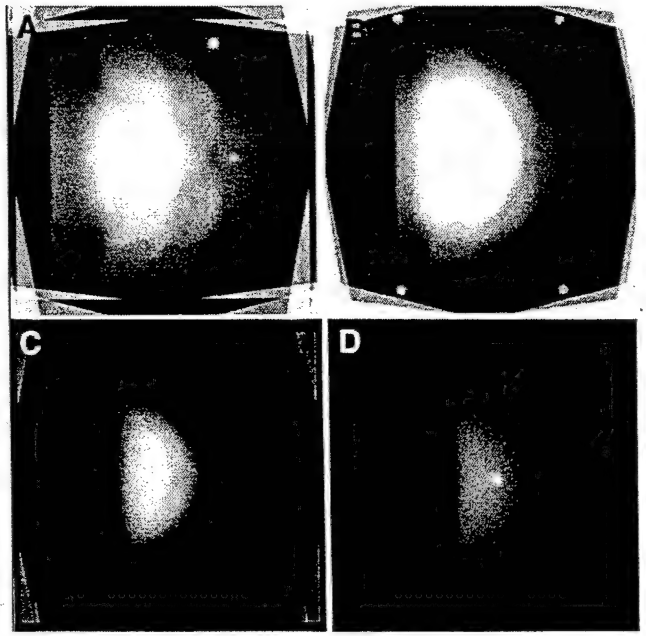

FIGURE 4. Four of 40 ETACT reconstructed slices for case 10/10 (tumor diameter of 10 mm and 10:1 TNT) using 3-mm pinhole. (A) Fifth fiducial plane. (B) Four fiducials. (C) Random slice within breast. (D) Slice containing tumor.

other. Thus, the CNR should be indicative of lesion detectability just as SNR is.

Planar images were simulated for the 10/10 case (which refers to a 10-mm tumor and a TNT of 10:1) and varying pinhole size for comparison with the ETACT reconstructions. The straight lateral view of the breast was simulated with 7 times the counts in a single, simulated ETACT projection. In this way, the planar image had the same total counts as the total ETACT reconstruction. The contrast and the CNR for the planar case were compared with those of the ETACT reconstructed data.

Phantom Experiments

An 8 mm "tumor" was filled with ^{99m}Tc and inserted into the breast phantom (Data Spectrum Corp., Hillsborough, NC). The rest of the breast was filled with water and mixed with ^{99m}Tc to create a 10:1 TNT, 37 kBq/mL (1 mCi/mL) in the breast and 370 kBq/mL (10 mCi/mL) in the tumor. After the phantom was prepared, it was set on a table and 7 projections were taken with a portable gamma camera (TransCam; ADAC Laboratories, Milpitas, CA) using a pinhole collimator. The positioning of the 7 projections was taken to resemble those in the simulation study. Figure 5 displays the experimental setup. The TransCam camera has a 260-mm field of view and a 6.5-mm NaI crystal thickness. This camera has an intrinsic spatial resolution of 3.6 mm and an energy resolution of 10.9% at 140 keV. The data were acquired with a 15% energy window. A 4-mm pinhole was used. Each projection was acquired for 5 min. The total count for each projection was around 45,000. The TACT software was used to reconstruct the data as described. The contrast and CNR measurements were calculated in the same fashion as in the simulation study.

RESULTS

Simulation Results

The simulation results are presented in Tables 2 and 3 and in Figure 6. The labeling 10/5 refers to a tumor size of 10 mm and a TNT of 5:1, whereas 5/10 refers to a tumor size of 5 mm and a TNT of 10:1. Values for all 6 different pinhole sizes are listed. The contrast results are displayed in Table 2. The CNR results are shown in Table 3 and in Figure 6. Our results indicate that a CNR of around 2 is the threshold for detectability. In each case, there is an optimal peak in the CNR curve. The overall optimum is a 3-mm pinhole for a tumor of size 10 mm and a TNT of 10:1. The highest concentration of the best CNRs is as a result of the 3-mm pinhole. Figure 4 shows 4 reconstructed simulations for the 10/10 case. Table 4 compares the contrast and CNR of the planar and ETACT simulations as a function of pinhole size. In all cases, the contrast and CNR for the planar case were less than those for the ETACT case, primarily because of the increased contrast that resulted from the ETACT reconstruction.

TABLE 2
Contrast Measurements

Pinhole size (mm)	Contrast					
	10/10	7.5/10	5/10	10/5	7.5/5	5/5
1	0.472	0.283	0.123	0.254	0.16	0.055
2	0.454	0.262	0.1	0.226	0.145	0.066
3	0.437	0.231	0.068	0.199	0.094	0.049
4	0.375	0.176	0.059	0.149	0.088	0.057
5	0.256	0.148	0.05	0.145	0.078	0.066
6	0.206	0.099	0.055	0.097	0.063	0.058

Case 10/10 refers to 10-mm tumor size and TNT of 10:1, whereas case 7.5/5 refers to 7.5-mm tumor size and TNT of 5:1.

Phantom Results

The results of the phantom experiment including the 8-mm tumor are given in Table 5. Reconstructed slices through the breast, including the fifth marker, the 4 coplanar markers, the breast, and the tumor, are shown in Figure 7. The 8-mm tumor is detectable and these results are comparable with our simulation results.

DISCUSSION

In the simulation experiments, ETACT was shown to have the potential of detecting tumors <1 cm. However, a

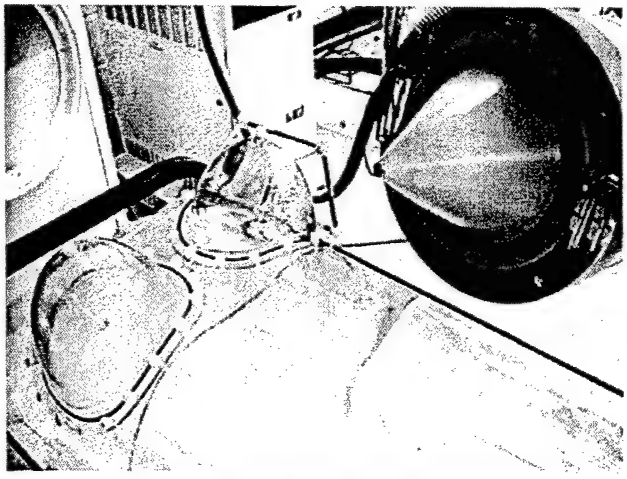

FIGURE 5. Phantom experiment setup includes anthropomorphic phantom and portable gamma camera with pinhole collimator aimed at lateral side of breast. Seven projections were taken of breast at different angles. These projections were then reconstructed using ETACT software to create slices through breast.

TABLE 3
CNR Measurements

Pinhole size (mm)	CNR					
	10/10	7.5/10	5/10	10/5	7.5/5	5/5
1	4.63	2.77	1.21	2.5	1.57	0.54
2	6.98	4.03	**1.54**	3.48	**2.23**	1.02
3	**8.57**	**4.53**	1.33	**3.9**	1.84	0.96
4	7.98	3.74	1.26	3.17	1.87	1.22
5	6.24	3.61	1.22	3.53	1.9	1.61
6	5.72	2.75	1.53	2.7	1.75	**1.61**

Optimum for each case is in boldface type.

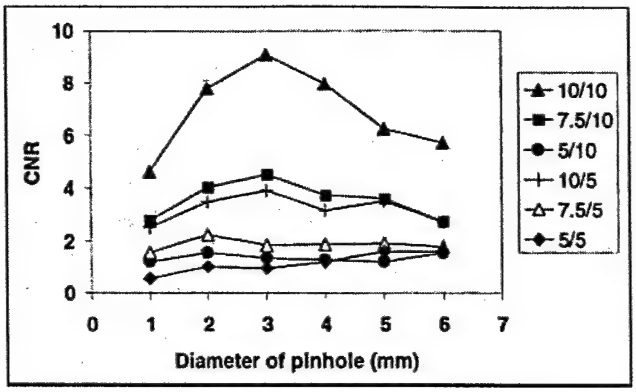

FIGURE 6. Plot of CNR measurements for different simulated cases: as TNT increases, CNR also increases. In most cases, optimal pinhole size is 3 mm.

5-mm tumor was not detectable even for a TNT as high as 15:1. The CNR threshold for detection was determined objectively to be around 2.0. As the pinhole size of the collimator increased, the contrast of the image worsened and the noise decreased; conversely, as the pinhole size decreased, the contrast improved and the noise worsened. Thus, there may be an optimal pinhole size as determined by that that yields the maximal CNR. The optimal pinhole size was observed to be the 3-mm pinhole for all discernable cases, although it was not substantially better than 4 mm. The contrast and CNR were consistently higher for the ETACT simulation compared with a planar simulation.

The simulation study may be limited because attenuation and Compton scatter were not included in the model. Attenuation may have an effect on the final image. γ-Rays from the tumor had to travel half of the breast, but γ-rays from behind the tumor had more tissue through which to travel and thus would be attenuated more. Attenuation may have reduced the image contrast, but the effect would probably be small. In Compton scatter, the photon changes direction as it scatters, causing a loss in spatial resolution and the contrast for small objects to worsen. In the clinic, the limited energy resolution of the NaI crystal in the gamma camera makes it impossible to eliminate all of the Compton scattering. Even with a 15% energy window, scattered radiation will still be incorporated into the image. Therefore, the phantom study results may not exactly match

TABLE 4
Comparison of Simulated Planar and ETACT Data

Pinhole size (mm)	Contrast		CNR	
	Planar	ETACT	Planar	ETACT
1	0.402	0.472	3.98	4.63
2	0.345	0.454	5.43	6.98
3	0.300	0.437	5.58	8.57
4	0.255	0.375	5.13	7.98
5	0.214	0.256	4.40	6.24
6	0.165	0.206	3.25	5.72

TABLE 5
ETACT Phantom Results

Tumor size (mm)	Phantom measurements		
	Contrast	% SD	SNR
8	0.58	15.8	3.67

Measurements were made with 4-mm pinhole.

the simulated data because of attenuation and Compton scatter. On the other hand, it is unclear whether the inclusion of attenuation and Compton scatter has much effect on the comparison of ETACT with other conventional imaging methods because these considerations would affect these methods as well. We are investigating the role of attenuation and Compton scatter in ETACT through Monte Carlo simulations and a comprehensive phantom study.

In the phantom studies, the aim was to create a simulated clinical setting. The breast was filled with a 37-kBq/mL (1 mCi/mL) solution and the tumor was filled with 370 kBq/mL (10 mCi/mL). The phantom was imaged with seven 5-min exposures, a total of 35-min acquisition time, which would be considered a reasonable study time in the clinic. The phantom results are a reasonable indication of what may be expected with real patient data. The phantom results also verified the validity of the simulation results.

To improve the potential of the ETACT method, some aspects of the experimental setup need further investigation:

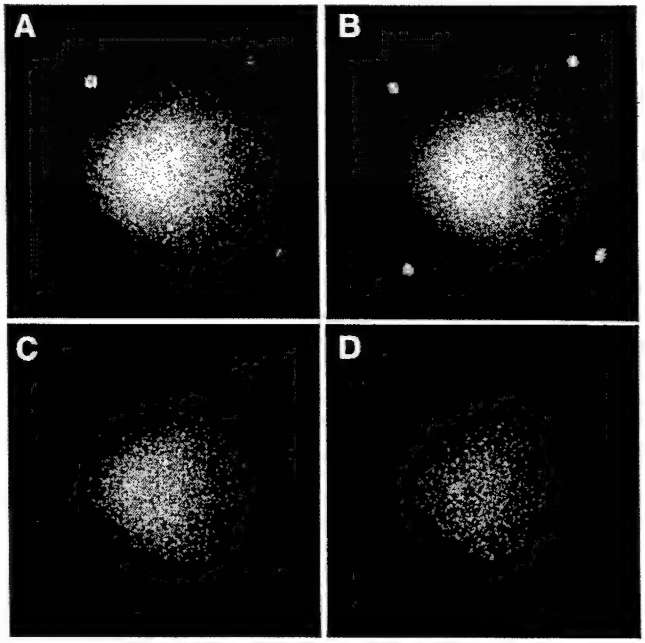

FIGURE 7. Four of 40 reconstructed slices of anthropomorphic phantom using 8-mm tumor size with 10:1 TNT. (A) Fifth fiducial slice. (B) Four fiducials. (C) Random slice within breast. (D) Slice containing 8-mm tumor. As viewed, 8 mm is detectable.

pinhole size, collimator, field of view, angular disparity of the projections, and iterative deconvolution. On the basis of our simulation results, a 3-mm pinhole will be constructed and used for future phantom studies. Simulation results imply that a 6-mm tumor might be visible with the 3-mm pinhole. Another way of improving the resolution, and therefore the SNR, of the images is to increase the field of view of the detector, allowing for more magnification. This could possibly be accomplished by the use of optical markers. Instead of radioactive fiducial markers, visible ones could be used with an optical system mounted to the gamma camera. The optical markers would be used for the reconstruction process. Thus, the gamma camera could more closely approach the patient with more flexibility, but without all of the fiducial markers necessarily being in the field of view of the gamma camera. This could lead to an increase in both resolution and sensitivity. Iterative deconvolution could also improve the results of the ETACT method, by subtracting the unwanted signals from neighboring slices. To fully analyze the ETACT method, a clinical evaluation needs to be performed eventually.

CONCLUSION

We evaluated the scintimammography technique, ETACT, through simulation and phantom experiments. The simulation experiments revealed that the 3-mm pinhole size is the optimum for the best tradeoff between resolution and noise. The phantom studies were consistent with the simulation results and proved that we can get reasonable results in a simulated clinical setting. In the phantom experiments, the 8-mm tumor was visible using the 4-mm pinhole. Therefore, ETACT has the potential to improve patient diagnoses by detecting tumors at an earlier stage and could be applied in any hospital in an easy and flexible manner.

ACKNOWLEDGMENTS

The authors thank Cathy Eades and Zhiping Mu for their help in the performance of these studies. The U.S. Army Medical Research and Materiel Command under DAMD grant 17-98-8349 supported this work.

REFERENCES

1. Overmoyer B. Breast cancer screening. *Med Clin North Am.* 1999;83:1443–1466.
2. Hannon D. Breast imaging: fighting a good fight. *Med Imaging.* 1999;14:38–43.
3. Fraumeni JF Jr, Hoover RN, Devesa SS, Kinlen LJ. Epidemiology of cancer. In: DeVita VT, Hellman S, Rosenberg SA, eds. *Cancer: Principles and Practice of Oncology.* 4th ed. Philadelphia, PA: JB Lippincott; 1993:150–181.
4. Neumann P, Romann D, Camara O, Riedel HH. Possibilities and limits of mammography with special reference to breast carcinoma: a comparison of clinical, mammography and histologic diagnoses [in German]. *Zentralbl Gynakol.* 1997;119:154–159.
5. Khalkhali I, Cutrone J, Mena I, et al. Technetium-99m-sestamibi scintimammography of breast lesions: clinical and pathological follow-up. *J Nucl Med.* 1995; 36:1784–1789.
6. Palmedo H, Schomburg A, Grünwald F, Mallmann P, Boldt I, Biersack HJ. Scintimammography with Tc-99m MIBI in patients with suspicion of primary breast cancer. *Nucl Med Biol.* 1996;23:681–684.
7. Webber RL, Horton RA, Tyndall DA, Ludlow JB. Tuned-aperture computed tomography (TACTTM): theory and application for three-dimensional dentoalveolar imaging. *Dentomaxillofac Radiol.* 1997;26:53–62.
8. Grant G. Tomosynthesis: a three-dimensional radiographic imaging technique. *IEEE Trans Biomed Eng.* 1972;1:20–28.
9. Webber RL, Underhill HR, Freimanis RI. A controlled evaluation of tuned-aperture computed tomography applied to digital spot mammography. *J Digit Imaging.* 2000;13:90–97.
10. Hemler PF, Webber RL, Fahey FH. Modeling and error identification of three dimensional tomosynthetic reconstructions. *SPIE Proc.* 2000;1287:1280–1287.
11. Sorenson JA, Phelps ME. *Physics in Nuclear Medicine.* 2nd ed. New York, NY: Grune & Stratton; 1987:342.

Biorthogonal merging of mammographic slices using Tuned-Aperture Computed Tomography®

Richard L. Webber
Departments of Dentistry and Medical Engineering, Division of Radiologic Sciences
Wake Forest University School of Medicine
Winston-Salem, NC 27157-1093
rwebber@wfubmc.edu

Frederic H. Fahey
Department of Medical Engineering
Wake Forest University School of Medicine
Winston-Salem NC 27157-

This investigation demonstrates a method for creating three-dimensional (3D) mammograms. It involves biorthogonal merging of independent tomographic representations. A test specimen containing human breast tissue with reference points attached was irradiated from five angles and from two orthogonal orientations. Data from both orientations were processed independently to yield data derived from the same tissues but oriented orthogonally. By combining suitably-corrected 3D matrix representations of these data, it was possible to assign more accurate estimates of volume elements in the resulting 3D reconstructions. Data obtained using a conventional digital stereotactic mammography system yielded a merged 3D image that retained spatial details and apparent structural continuity even when rendered as a cube rotated through a full 360•. We conclude that merging 3D matrices derived from multiple projections obtained biorthogonally may offer an intriguing alternative to conventional 2D digital mammography and intrinsically anisotropic 3D mammographic imaging methods.

KEY WORDS: digital imaging, three dimensions, mammography, computed tomography, nonlinear processing

Sent to Journal of Electronic Imaging

ABSTRACT

This investigation explores the potential for creating three-dimensional (3D) mammograms through biorthogonal merging of independent tomographic representations. A cuboidally shaped test specimen containing human breast tissue with reference points attached to each corner was irradiated from five angles and from two orthogonal orientations, yielding a total of 10 projections. Data from both orientations were processed independently to yield independent laminographic series derived from the same tissues but oriented orthogonally. Relationships derived from respective projections of the reference points were used to correct for cone-beam artifacts. A matrix-rotation program was developed and applied to the data underlying one of these now affine-corrected 3D representations that, in effect, flipped it 90•. By combining the rotated 3D volume representation with its unrotated, orthogonally generated counterpart, it was possible to assign more accurate estimates of volume elements in the resulting 3D reconstructions. Data obtained using a conventional digital stereotactic mammography system yielded a merged 3D image that retained spatial details and apparent structural continuity even when rendered as a cube rotated through a full 360•. We conclude that merging 3D matrices derived from multiple projections obtained biorthogonally may offer an intriguing alternative to conventional 2D digital mammography and intrinsically anisotropic 3D mammographic imaging methods.

1 Introduction

Conventional mammography is an intrinsically two-dimensional (2D) imaging process. As such, its diagnostic potential is necessarily limited by the extent to which essential 3D information is obscured by irrelevant tissue details located either above or below the region of interest. The similarity in attenuation between normal and cancerous breast tissues affects both sensitivity and specificity and is particularly important when the region of interest is small and the enveloping tissue relatively dense. The addition of depth information via conventional stereometry has been shown to improve diagnostic

performance.[1] However, this approach does not allow for suppression of 3D details known to be irrelevant (structured noise).[2]

Conventional computed tomography (CT) provides a theoretically tractable means for isolating questionable tissue patterns in 3D, but anatomical and radiographic restrictions unique to mammographic applications present a formidable challenge to existing CT scanner designs.[3,4] Recent findings by Niklason *et al.*[5] suggest that digital tomosynthesis may provide significant benefits for breast cancer screening. This conclusion was reinforced by the results of a controlled in vitro study demonstrating significantly improved sensitivity for detection of standardized mammography details buried in normal breast tissues when displayed in 3D.[6] However, off-axis projection constraints required by tomosynthetic imaging geometry necessarily induce spatial correlations between reconstructed slices, thereby restricting 3D information to regions outside the associated null space.

2 Experimental Goal

This investigation explores a method for effectively eliminating this shortcoming through the merging of data produced by using multiple orthogonal sampling strategies. More specifically, we test the hypothesis that it is possible to combine data obtained from two (or more) tomosynthetic projection series oriented at right angles to each other to yield a single composite 3D representation that minimizes the sampling gaps associated with the intrinsic "one-sided" reconstruction techniques underlying conventional tomosynthesis.

3 Theoretical Considerations

Before we can achieve this objective, we must solve some technical problems. One such problem is caused by the cone-beam projection geometry used to produce the underlying source projections. All projections produced from a finite focal-object distance necessarily exhibit significant differences in projective magnification from one slice to the next. For this reason, details in planes relatively nearer the x-ray source are magnified more than comparable details located nearer the projection plane. Consequently, a volume that in reality has the shape of a cube appears as a truncated pyramid when rendered tomosynthetically in 3D (Fig.1).

This intrinsic scaling distortion poses no significant problems so long as each slice is interpreted independently. However, when slices produced from conventional projection sequences are to be registered with others synthesized from orthogonally oriented samples, even relatively small variations in projection scaling with depth can preclude accurate spatial registration. We chose to avoid this difficulty by isotropically rescaling each reconstructed slice by an amount calculated to produce unity magnification throughout the volume. Because the results are identical to those that would have been produced using affine projection geometry, we coined the term "affinization" to describe this correction procedure.[7]

Another problem that must be solved is the need for precise registration of homologous volume elements. We dealt with this problem by attaching easily recognized fiducial points to the object of interest. Because these points were positioned in fixed known locations, the affinization process described

above was easy to perform. Moreover, the reconstruction process was rendered more precise by eliminating any projection inaccuracies associated with rigid coupling of the object to the projection system. This simplification arises from the use of these same fiducial points to accomplish the 3D reconstruction using Tuned-Aperture Computed Tomography® in lieu of conventional tomosynthesis.[8,9] Finally, precise registration of the two resulting affinized 3D volumes was accomplished through the straightforward process of projective superposition.

4 Materials and Methods

This approach was used to image some frozen human breast tissue known to contain calcified blood vessels and characteristic microcalcifications. Multiple slices of this tissue ranging in thickness from 10 to 12 mm were stacked and cut into squares that would fit snugly into a 35 mm cardboard film box measuring 38 x 38 x 53 mm. Lead spheres approximately 2 mm in diameter (Y-Spots, Beekley Corp., Bristol, CT USA) were attached to the four bottom corners of the box, and four more were attached to the vertical edges at a distance 38 mm up from the base. This procedure yielded a cube-shaped region containing frozen breast tissue bounded at each vertex by easily recognized radiopaque markers (Fig. 2).

This container was radiographed as shown in Fig. 2 from five discrete angles using a modified mammography machine configured with a swing arm and a digital camera attachment used in stereotactic applications (Delta 16, Instrumentarium Imaging, Tuusula, Finland). Note that the position of the box was shifted laterally slightly between successive exposures to assure that all eight fiducial reference points were always projected onto the region defined by the digital detector when the position of the x-ray source changed. The resulting mammographic projections had angular disparities of approximately -15°, -7.5°, 0°, 7.5°, and 15° from vertical. Five anteroposterior (AP) images were obtained under these conditions using default settings for kVp and exposure as determined by the automatic exposure system on the machine. The box then was rotated 90° about an axis perpendicular to the front and rear faces of the cube, and the lateral projection series (LAT) was repeated using the same settings. This procedure yielded the two orthogonal projection sets shown in Fig. 3.

These two orthogonal sets were used to produce two independent series of 165 tomosynthetic slices each. To minimize the introduction of known tomosynthetic artifacts into the reconstruction of individual slices caused by unregistered projections of high-contrast structures located outside the plane of

interest, we used two different deblurring techniques, one linear and one nonlinear. The linear method involved the application of an iterative deconvolution scheme based on the known point-spread function underlying the 3D reconstruction process.[10] The nonlinear method involved minimization of respective pixel values as opposed to the averaging process underlying conventional back-projection algorithms.[11] It has been suggested that this expedient may increase observer specificity for radiopaque signals at the expense of sensitivity.[12] As described above, these slices were then affinized individually by proportional re-projection of each, relative to fixed positions established by the shadows produced from the four coplanar fiducial points located closest to the plane of the digital detector. Slight inaccuracies caused by the imperfect placement of the fiducial points on the exact corners of a cube, likewise, were corrected in this way, thus assuring that each slice within the confines of the cube was remapped into a perfect square. Cropping each resultant 3D matrix (stack of slices) to only the volume enclosed by the cube produced two independent representations of the same volume from the two original orthogonal projection sets. Shifting corresponding voxel addresses from one matrix such that they reference homologous volume elements in the other permitted merging of these independent data sets through simple averaging of corresponding slices. The resulting 3D matrices were then rendered using either linear averaging or nonlinear maximum-brightness ray-tracing schemes. The results were a series of conventional-appearing 2D projections that could be selected interactively or displayed in rapid sequence through a series of contiguous angles spanning a full 360°.

5 Results

Fig. 4 shows a series of representative projections produced using a maximum-brightness rendering scheme generated from the merged 3D data and from both unmerged 3D components. For these examples the underlying slice reconstructions were the result of linearly deconvoluted back projections. They are arranged in such a way that each row shows the effect of a 90° rotation through an increment of 45°. The middle row illustrates the effect of merging the 3D matrices seen in the top and bottom rows produced from the AP and LAT orthogonal data sets, respectively. Notice that the interslice correlations produced from the limited angular disparity associated with tomosynthetic sampling geometries create large streak artifacts. These are particularly evident when the 3D reconstructions are viewed at angles significantly greater (45° and 90°) than the maximum disparity of the source projections (30°) underlying

each of the separate orthogonally sampled matrices. The superiority of the projections produced from the merged data (middle row) is obvious, especially when compared with Figs. 4(b) and 4(c) (top row) and 4(g) and 4(h) (bottom row). Notice also the significant artifactual streaking of the high-contrast structures caused by the linear back-projection reconstruction method even in 4(a) and 4(i), the unrotated, optimally projected images.

These artifacts appear much less obvious in the comparable projections shown in Fig. 5. The only difference between these renderings and those seen respectively in Fig. 4 is the use of the nonlinear minimization algorithm described above instead of iteratively deconvoluted linear back projections for the underlying 3D image reconstructions. Although these images contain fewer obscuring streak artifacts than those seen in Fig. 4, by virtue of their intrinsic nonlinearity they necessarily introduce significant errors of omission that may, or may not, interfere with image interpretation depending on the diagnostic task involved. Indeed, the nonlinear methods used to accomplish the merging process as demonstrated above necessarily reject most of the information produced from the 10 basis projections.

The results displayed in Fig. 6 illustrate the opposite effect. Here, the reconstructions and renderings were accomplished using all linear methodology. This is to say that the merged reconstructions were derived from iteratively deconvoluted back projections, and the resulting projections were rendered using averaging in lieu of the maximum brightness algorithm underlying the displays shown in Fig. 4. Notice the relative retention of fixed-pattern artifacts intrinsic to redundant projective sampling geometry in Fig. 6. For example, these blurring artifacts tend to obscure the calcified blood vessel and other diagnostic details in projections rotated significantly from the projection geometry underlying the original source projections.

6 Discussion

Irrespective of the choice of algorithms selected for 3D reconstruction and display, these results appear to be consistent with our hypothesis that artifacts produced by anisotropic sampling intrinsic to tomosynthetic projection geometries can be mitigated through redundant sampling made possible by integration of multiple data sets. Limiting redundant samples to mutually orthogonal projection geometries as demonstrated in this investigation also assures that the number of required projections for anisotropic sampling can be minimized. However, there is no theoretical restriction of this approach for minimizing

null spaces that limits the merging of 3D data to those produced solely from orthogonal projection geometries. Indeed, any sampling scheme that permits independent estimates of a common 3D volume to be realized can be conceivably integrated into a more uniform and, hence, less distorted 3D representation.

In this instance one can opt to use conventional linear reconstruction and rendering methods that theoretically retain most of the information contained in the source projections but often obscure desired details with the intrinsic tomographic blur associated with correlated image sampling within a given projection series. Alternatively, one can employ one or more nonlinear processing options that necessarily reduce the relative amount of information retained with the intent that their use also excludes undesired information such as correlated blur produced from out-of-focus structures. As demonstrated in Figs. 4, 5, and 6, either option can yield improved 3D image quality at extreme angles through the expedient of biorthogonal merging of independently sampled sets of projection data.

The residual streaking of high-contrast structures from the merged data (middle rows of Figs. 4, 5, and 6) is likely aggravated by the fact that the total angular disparity (30°) used to produce each component projection set does not encompass the entire range of projection angles (see Fig. 7). We are currently testing this hypothesis in another radiographic application by using a more uniform sampling strategy involving biorthogonal merging, wherein the use of angular disparities approaching the required 90° is more easily accomplished.

We also recognize that the simple merging technique demonstrated here most likely is not optimized for many, if not most, common mammographic applications. We suspect, for example, that sophisticated strategies based on maximum likelihood criteria might be more appropriate for certain specific detection tasks. Again, we plan to explore such task-specific options more rigorously in the future.

7 CONCLUSIONS

We have demonstrated that it is possible to combine 3D information, derived from two independent orthogonally oriented sets of x-ray projections, into a single unified 3D image that can be visualized from any angle with fewer of the intrinsic correlation artifacts associated with conventional tomosynthetic reconstruction schemes. Moreover, the use of nonlinear methods for reconstruction and display of the resulting merged 3D information can produce sharp-appearing renderings from a broad range of angles that appear to be all but clinically uninterpretable when rendered by conventional back-projection

algorithms. However, rational interpretation of the relatively blur-free nonlinearly processed images as demonstrated here is appropriate only for specific diagnostic tasks that can be shown to be uninfluenced by the inevitable information losses associated with these filtering schemes.

Acknowledgment

This work was supported in part by National Institutes of Health Grant No. 5 RO1 CA74106.

References

1. M. May, "Three-dimensional mammography," *Am. Scientist* 82, 421-422 (1994).
2. H. L. Kundel and G. Revesz, "Lesion conspicuity, structured noise, and film reader error," *AJR Am. J. Roentgenol.* 126, 1233-1238 (1976).
3. S. L. Edell and M. D. Eisen, •Current imaging modalities for the diagnosis of breast cancer," *Del. Med. J* . 71, 377-382 (1999).
4. J. W. T. Muller, P. F. G. M. van Waes, P. R. Koehler, "Computed tomography of breast lesions: comparison with x-ray mammography, " *J. Comput. Assist. Tomogr.* 7, 650-654 (1983).
5. L. T. Niklason, B.T. Christian, L. E. Niklason, D. B. Kopans, D. E. Castleberry, B. H. Opsahl-Ong, C. E. Landberg, P. J. Slanetz, A. A. Giardino, R. Moore, D. Albagli, M. C. DeJule, P. F. Fitzgerald, D. F. Fobare, B. W. Giambattista, R. F. Kwansnick, J. Liu, S. J. Lubowski, G. E. Possin, J. F. Richotte, C. Y. Wei, R. F. Wirth, "Digital tomosynthesis in breast imaging," *Radiology* 205, 399-406 (1997).
6. R. L. Webber, H. R. Underhill, R. I. Freimanis, "A controlled evaluation of tuned-aperture computed tomography applied to digital spot mammography," *J. Digit. Imag.* 13, 90-97 (2000).
7. T. M. Persons, P. F. Hemler, R. L. Webber, H. R. Underhill, "Elimination of tomosynthetic artifacts through integration of orthogonal volume sets," *Medical Imaging 1999: Physics of Medical Imaging*, Proc. SPIE 3659, 925-932 (1999).
8. Webber RL, inventor; Wake Forest University, assignee; "Self-calibrated tomosynthetic, radiographic-imaging system, method and device," US patent 5,359,637 (1994 Oct 25).
9. Webber RL, inventor; Wake Forest University, assignee; "Self-calibrated tomosynthetic, radiographic-imaging system, method and device," US patent 5,668,844 (1997 Sept 16).

10. U. E. Ruttimann, R. A. J. Groenhuis, R. L. Webber, "Restoration of digital multiplane tomosynthesis by a constrained iteration method," *IEEE Transactions on Medical Imaging*, MI-3, 141-148 (1984).

11. R. L. Webber, P. F. Hemler, J. Lavery, "Objective evaluation of linear and nonlinear tomosynthetic reconstruction algorithms," *Medical Imaging 2000: Technology Evaluation and Observer Performance*, Proc. SPIE 3981, 224-231 (2000).

12. R. L. Webber, H. R. Underhill, P. F. Hemler, J. Lavery, "A nonlinear algorithm for task-specific tomosynthetic image reconstruction," *Medical Imaging 1999: Physics of Medical Imaging*, Proc. SPIE 3659, 258-265 (1999).

FIGURE CAPTIONS

Fig. 1 Diagram showing distortion of 3D shape produced by cone-beam projection geometry.

Fig. 2 Diagram showing projection geometry and detail of the breast specimen encased in a cube-shaped container with fiducial markers.

Fig. 3 Two independent series of five x-ray projections of the breast specimen, one oriented predominantly anteroposteriorly showing a calcified blood vessel (left column), and the other oriented predominantly laterally showing multiple adjacent layers of breast tissue (right column).

Fig. 4 Three series of linearly reconstructed (back-projected) images rendered with a nonlinear (maximum-brightness) ray-tracing scheme shown at various angles comparing images produced with and without biorthogonal merging.

Fig. 5 Three series of nonlinearly reconstructed (minimized) images rendered with a nonlinear (maximum-brightness) ray-tracing scheme shown at various angles comparing images produced with and without biorthogonal merging.

Fig. 6 Three series of linearly reconstructed (back-projected) images rendered with a linear (average) ray-tracing scheme shown at various angles comparing images produced with and without biorthogonal merging.

Fig. 7 Diagram showing undersampled regions produced by the 30° angle associated with the projection geometries underlying all of the 3D reconstructions in this report.

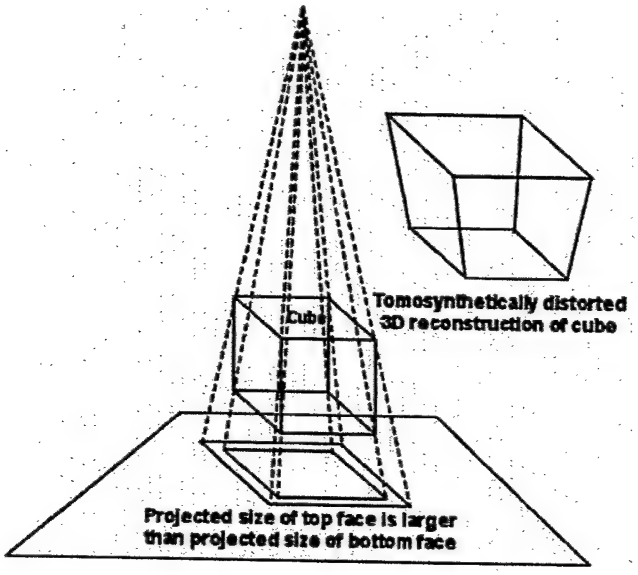
Tomosynthetically distorted
3D reconstruction of cube
Cube
Projected size of top face is larger
than projected size of bottom face

Fig. 1

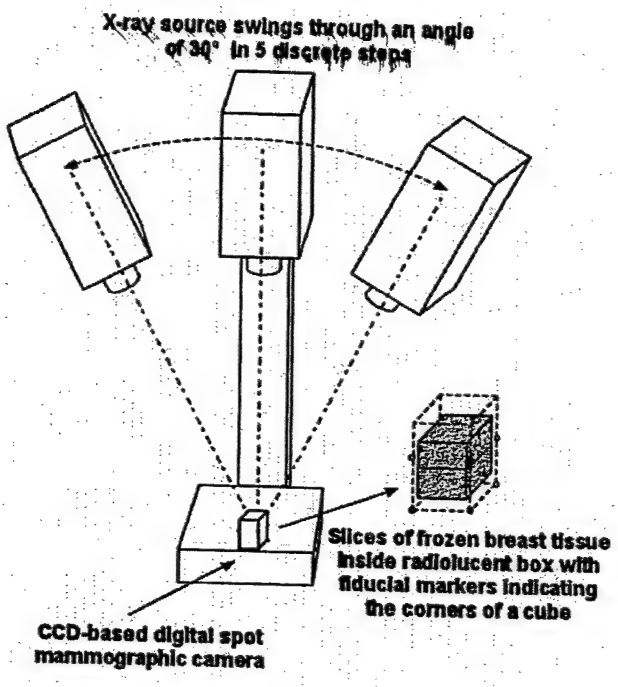
X-ray source swings through an angle of 30° in 5 discrete steps
Slices of frozen breast tissue inside radiolucent box with fiducial markers indicating the corners of a cube
CCD-based digital spot mammographic camera

Fig. 2

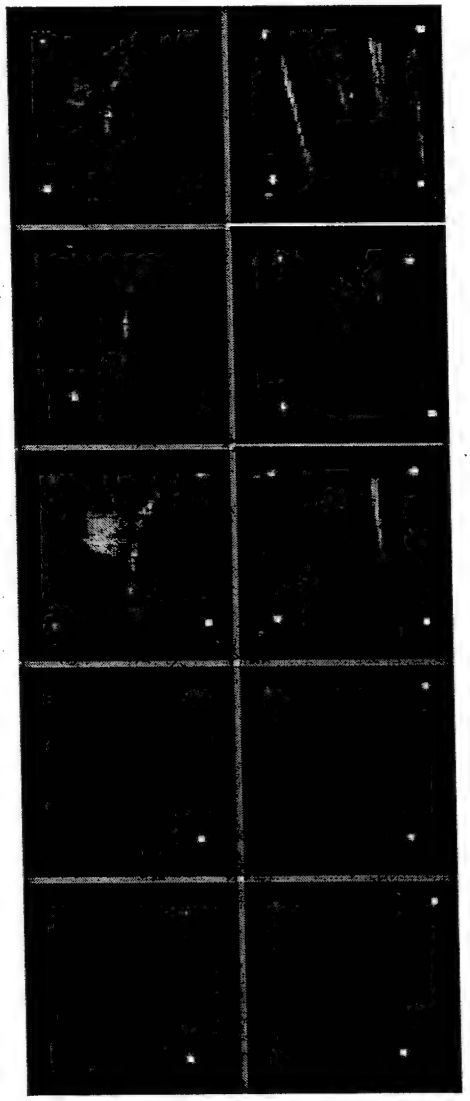

Fig. 3

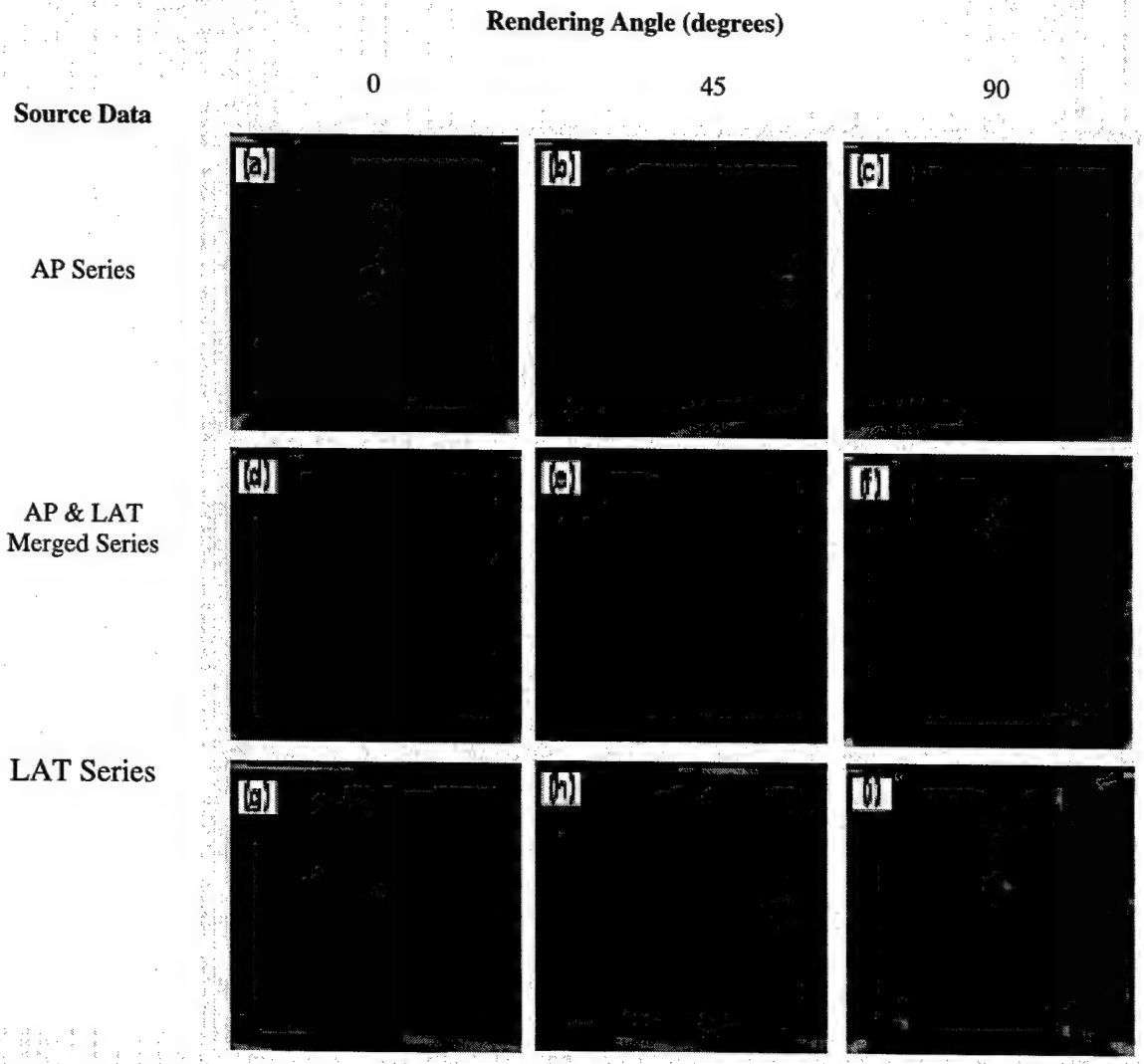
Rendering Angle (degrees)
0
45
90
Source Data
AP Series
AP & LAT
Merged Series
LAT Series
[a]
[b]
[c]
[d]
[e]
[f]
[g]
[h]
[i]

Fig. 4

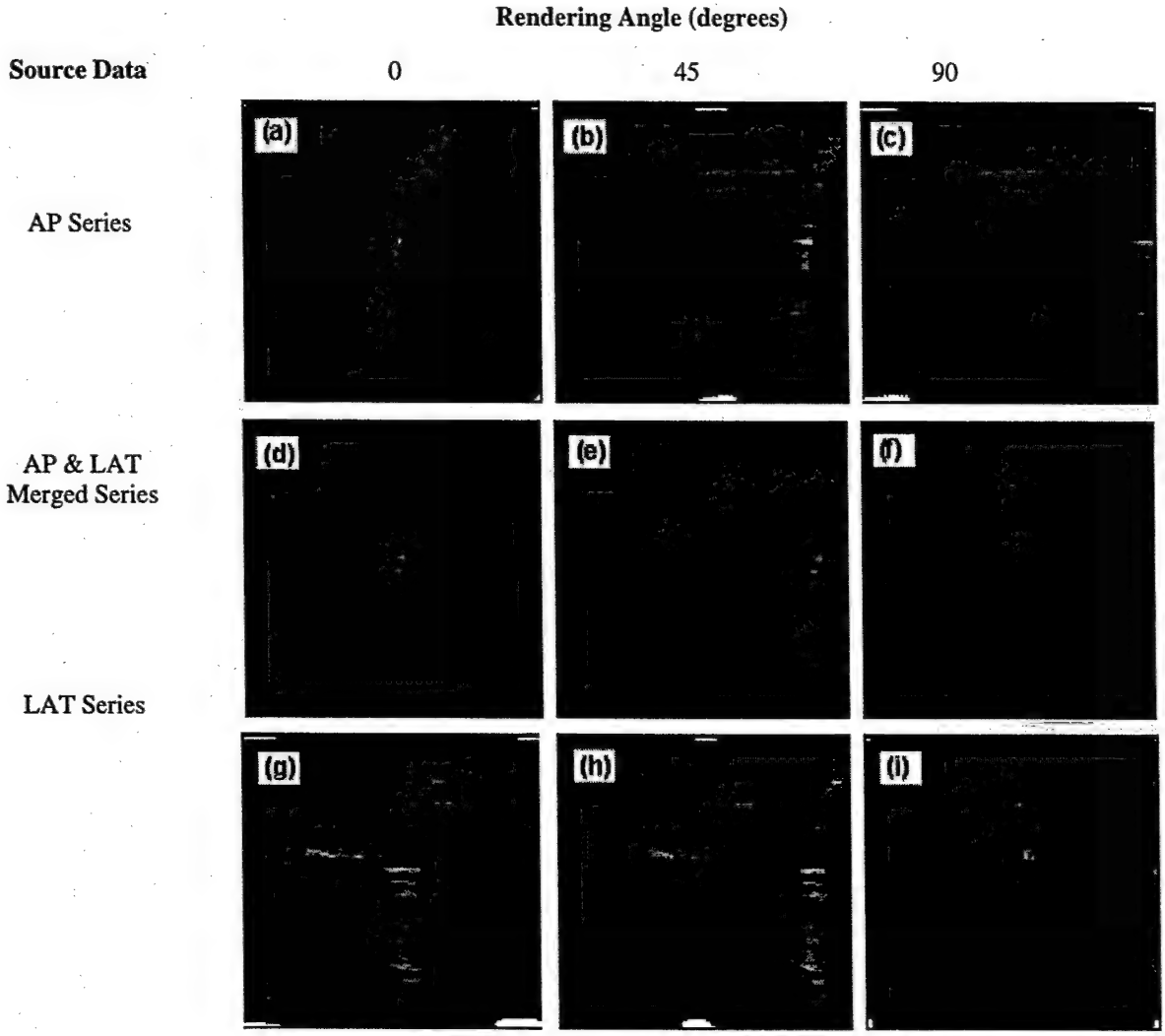
Rendering Angle (degrees)
Source Data
0
45
90
AP Series
AP & LAT Merged Series
LAT Series
(a)
(b)
(c)
(d)
(e)
(f)
(g)
(h)
(i)

Fig. 5

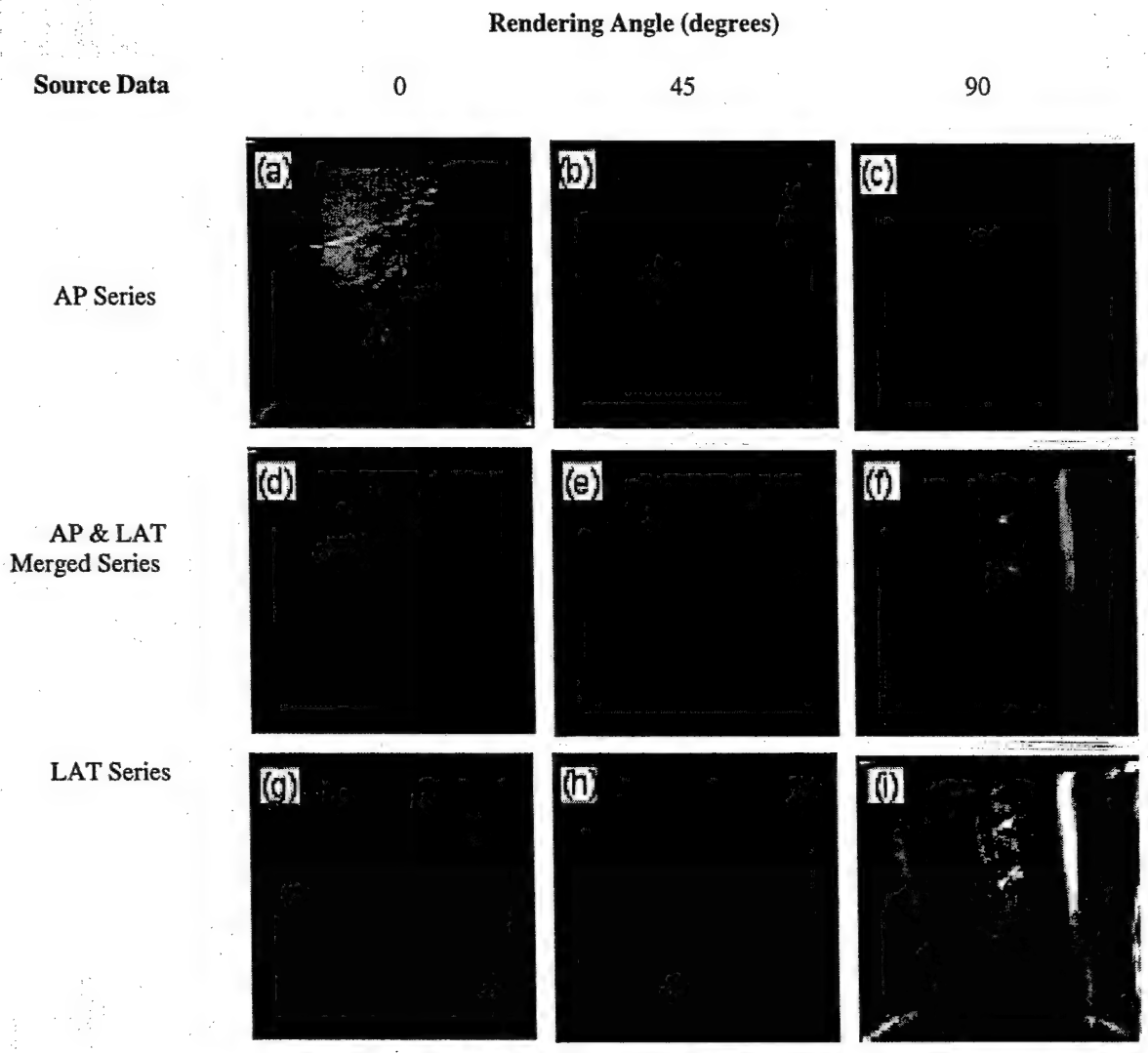
Rendering Angle (degrees)
Source Data
0
45
90
AP Series
AP & LAT Merged Series
LAT Series
(a)
(b)
(c)
(d)
(e)
(f)
(g)
(h)
(i)

Fig. 6

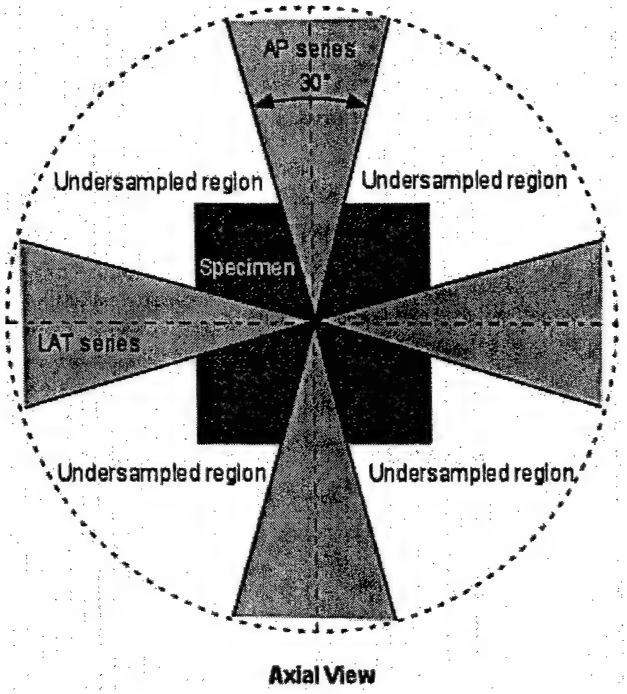
AP series
30°
Undersampled region
Undersampled region
Specimen
LAT series
Undersampled region
Undersampled region
Axial View

Fig. 7

Angular disparity in ETACT scintimammography

Frederic H. Fahey[a)]
Division of Radiologic Sciences, Wake Forest University School of Medicine, Winston-Salem, North Carolina 27157

Kerry L. Rhyasen
Department of Physics, Wake Forest University, Winston-Salem, North Carolina 27106

Beth A. Harkness
Division of Radiologic Sciences, Wake Forest University School of Medicine, Winston-Salem, North Carolina 27157

Michael A. Meltsner
Department of Physics, Wake Forest University, Winston-Salem, North Carolina 27106

Richard L. Webber
Division of Radiologic Sciences, Wake Forest University School of Medicine, Winston-Salem, North Carolina 27157

(Received 12 December 2001; accepted for publication 6 June 2002; published 9 August 2002)

Emission tuned aperture computed tomography (ETACT) has been previously shown to have the potential for the detection of small tumors (<1 cm) in scintimammography. However, the optimal approach to the application of ETACT in the clinic has yet to be determined. Therefore, we sought to determine the effect of the angular disparity between the ETACT projections on image quality through the use of a computer simulation. A small, spherical tumor of variable size (5, 7.5 or 10 mm) was placed at the center of a hemispherical breast (15 cm diameter). The tumor to nontumor ratio was either 5:1 or 10:1. The detector was modeled to be a gamma camera fitted with a 4-mm-diam pinhole collimator. The pinhole-to-detector and the pinhole-to-tumor distances were 25 and 15 cm, respectively. A ray tracing technique was used to generate three sets of projections (10°, 15°, and 20°, angular disparity). These data were blurred to a resolution consistent with the 4 mm pinhole. The TACT reconstruction method was used to reconstruct these three image sets. The tumor contrast and the axial spatial resolution was measured. Smaller angular disparity led to an improvement in image contrast but at a cost of degraded axial spatial resolution. The improvement in contrast is due to a slight improvement in the in-plane spatial resolution. Since improved contrast should lead to better tumor detectability, smaller angular disparity should be used. However, the difference in contrast between 10° and 15° was very slight and therefore a reasonable clinical choice for angular disparity is 15°.
[DOI: 10.1118/1.1500396]

I. INTRODUCTION

Mammography has been shown to be an excellent screening tool for breast cancer. Although it has a high sensitivity, it has limited specificity.[1] In addition, the sensitivity of mammography is compromised for women with either dense breasts, breast implants, or scarring from previous procedures. Scintimammography using ^{99m}Tc labeled sestamibi has demonstrated both high sensitivity and specificity (93.7% and 87.8%, respectively) for tumors larger than 1.5 cm.[2] However, it provides only moderate sensitivity for tumors less than 1 cm in diameter.[3] Patients who are diagnosed with breast cancer at a localized stage experience a higher survival rate than those where the cancer has spread to distant sites.[4] Thus early detection is pivotal in the treatment of breast cancer.

Emission tuned aperture computed tomography (ETACT) is a three-dimensional (3D) approach to nuclear medicine imaging that has demonstrated the potential for detecting small tumors using scintimammography.[5] ETACT is based upon the tuned aperture computed tomography® (TACT) method developed for radiography by Webber *et al.*[6] In TACT, a series of projections is acquired at different viewing angles about the object of interest. These projections can be acquired from any number of arbitrary viewing angles. Several fiducial markers are used to infer the projection geometry. These may be anatomical landmarks that are easily visible on the projection images but are more commonly external markers fixed to the object. The only requirements for a successful TACT acquisition is that the markers be fixed to the object and that all of the markers be visible on each of the acquired projection images. By localizing these markers in the projection images, one can infer the projection geometry. The nature of the TACT reconstruction has been described previously.[6] TACT has been shown to be useful in a variety of medical applications including dentistry and mammography.[7,8]

In ETACT, the gamma camera is fitted with a pinhole collimator and radioactive point sources attached to the object are used as the fiducial markers. One configuration of markers that has been shown to work well is to have four

 0094-2405/2002/29(9)/1980/4/$19.00

markers that are coplanar and to have a fifth marker that is removed from this plane. A series of projections are acquired about the object. The fiducial markers are identified in each projection image, and based on these locations, the ETACT data are reconstructed as a series of parallel slices. The spacing of these slices is arbitrary and can be selected at the time of reconstruction. In general, these slices are selected to be parallel to the plane containing the four coplanar markers. The pinhole collimator aids in the detection of small tumors by providing high spatial resolution and by minimizing the effect of radioactivity located in organs behind the breast, such as the heart or the liver. In a previous investigation, a computer simulation and a phantom study indicated that ETACT provided higher contrast than planar imaging and that the optimum pinhole diameter was 3–4 mm.[5] However, other aspects of the ETACT data acquisition, such as the optimum choice of projection angles, have yet to be defined.

In some respects, ETACT is similar to the use of multi-pinhole collimators[9–12] and rotating slant-hole collimators[13–15] for tomography. In these instances, the choice of projections is fixed by the design of the collimator. In ETACT, the choice of projections is flexible and can be selected at the time of imaging. This can be based on knowledge of the object being imaged or on practical aspects such as accessibility to the patient. In addition, in ETACT, the original acquisition can be augmented with additional views if so desired. Multi-pinhole and rotating slant-hole collimators were initially proposed for myocardial perfusion imaging. Limited angle tomography is more suited for the detection of hot features such as a tumor within the breast than it is for the assessment of cold features as in the case of myocardial imaging. For these reasons, ETACT holds more promise than these earlier investigations into limited angle tomography.

In the previous ETACT study,[5] computer simulations were generated with seven projections of the breast: one central projection and the other six were evenly distributed in a hexagonal array 15° from the central projection. In this investigation, we sought to determine the effect of using a different angular disparity than 15°.

II. METHODS

We performed a simulation study to determine the effect of angular disparity on ETACT reconstruction. The object was modeled as a spherical tumor of variable size (5, 7.5 or 10 mm diameter) in the center of a hemispheric breast (15 cm diameter). The tumor-to-nontumor ratio (i.e., the activity concentration in the tumor divided by the activity concentration in the breast and denoted as "TNT") was modeled to be 5:1 and 10:1. Five fiducial markers were placed to the lateral side of the breast. Four of the markers were coplanar and formed a 5×5 cm square. The fifth marker was out of this plane by 1 cm. This 3D object was represented as a series of 40 parallel and equally spaced slices. Projections were generated using a ray-tracing technique.[16] We modeled the detector as a 50×50 cm square so that all projections, including the markers, were within the field of view. The pinhole-to-tumor distance and the pinhole-to-detector distances were 15 and 25 cm, respectively. Three sets of images were generated. In each set, the first projection was a straight lateral and the other six were acquired in a hexagonal pattern about the first, central projection. In the three image sets, the peripheral projections were 10°, 15°, and 20° from the central projec-

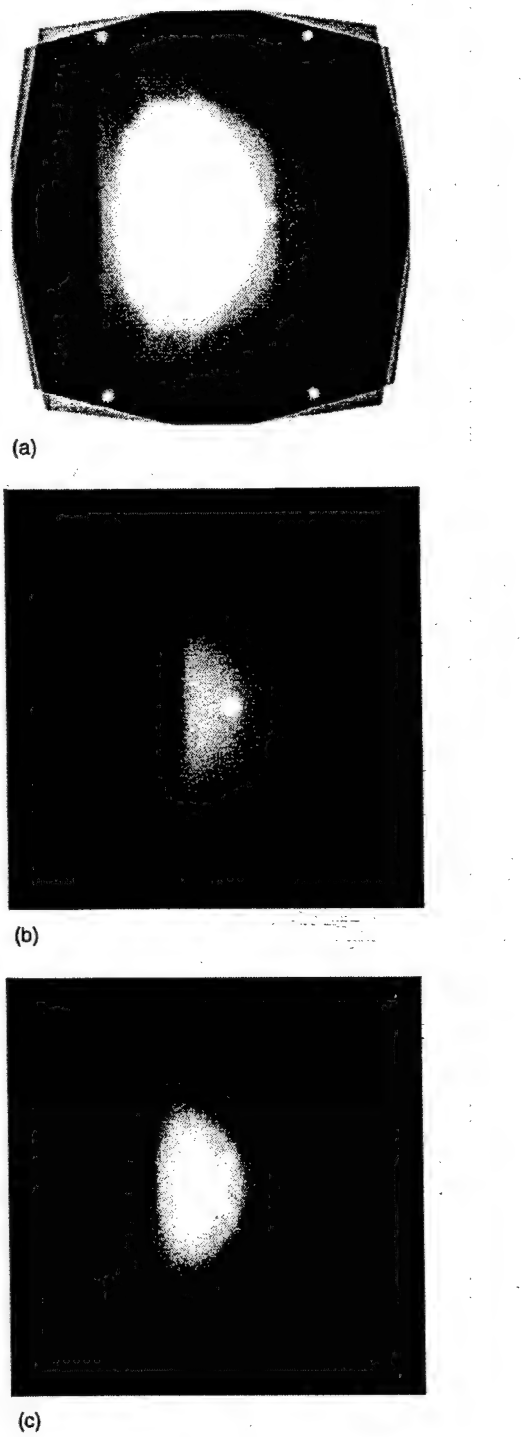

FIG. 1. TACT reconstructed slices through the simulated breast. (a) Slice through the four coplanar fiducial markers. (b) Slice through the simulated tumor. (c) Arbitrary slice through the breast.

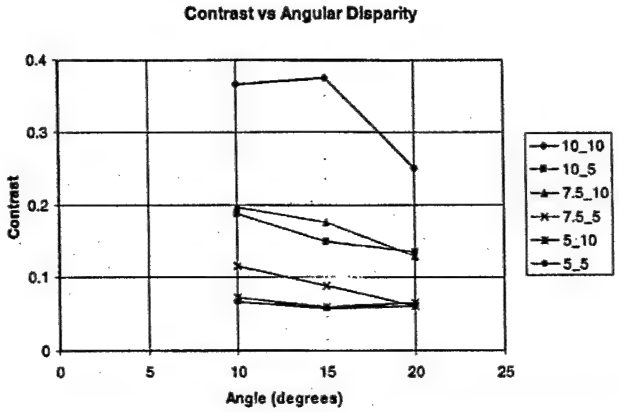

FIG. 2. Contrast vs angular disparity. Contrast of the simulated tumor is plotted against the angular disparity. Each curve represents a particular tumor configuration. For example, the curve denoted 7.5×10 represents the results for the 7.5 mm tumor with a 10:1 tumor to nontumor background.

tion, respectively. The resultant projections were blurred with a Gaussian kernel with a full width at half maximum (FWHM) of 4.52 mm, which is consistent with a 4 mm pinhole diameter, 3.5 mm intrinsic resolution, and the above-mentioned imaging geometry.

We reconstructed the data using the TACT software developed by Horton and Webber (Verity Software Systems, Winston-Salem, NC). In each case, the straight lateral was used as the reference image so that all three reconstructions were oriented in the same way. We analyzed the three image sets in a similar manner. The slice through the middle of the tumor was selected. A 16×16 pixel region of interest (ROI) was used to determine the counts over the tumor (TUM). Two similarly sized ROIs were placed adjacent to the tumor. The average of the counts in these two ROIs was considered background (BKG). The contrast (C) was estimated using the following formula:

$$C=\frac{(\mathrm{TUM}-\mathrm{BKG})}{\mathrm{BKG}}.$$

The axial distance over which an object converges after TACT reconstruction is referred to as the axial spatial reso-

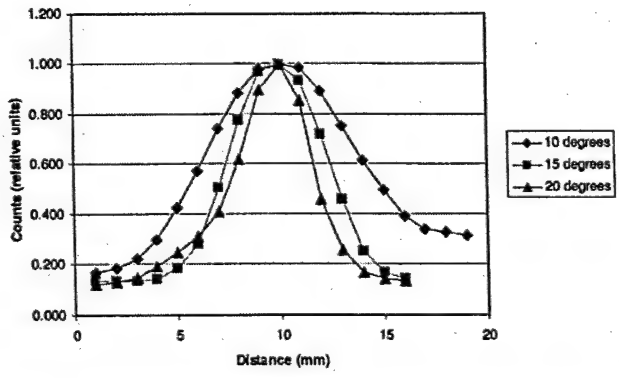

FIG. 3. Axial profiles curves. The axial profile, that is the plot of counts in a point source as a function of axial distance, is plotted for each angular disparity tested (10°, 15°, and 20°).

TABLE I. Axial spatial resolution vs angular disparity.

Angle (deg)	Axial resolution—FWHM (mm)
10	9.5
15	5.9
20	4.5

lution. A 16×16 pixel ROI was placed over one of the four coplanar point markers. The average counts in the ROI were noted as a function of slice number for the three angular disparities. We characterized the axial spatial resolution by using the FWHM of each resultant axial profile.

III. RESULTS

Figure 1 shows three of the ETACT reconstructed slices through the simulated breast: one through the plane containing the four coplanar markers, one through the middle of the simulated tumor, and one arbitrary slice through the breast. These data are for the 15° angular disparity case with a 10 mm tumor with 10:1 TNT. The excellent image quality associated with ETACT is demonstrated by the fact that the markers and the tumor are clearly resolved.

The contrast as a function of angular disparity for all combinations of tumor size and TNT is shown in Fig. 2. In general, it can be seen that the contrast decreases with increasing angular disparity. The loss in contrast is particularly noted for the 10 mm and 10:1 TNT ratio. In other cases, the contrast changes are more subtle. Figure 3 shows the axial count profiles for the three angular disparities. The axial spatial resolution as characterized by the FWHMs of these profiles is tabulated in Table I. These data indicate that the axial spatial resolution improves (that is, the FWHM decreases) with increasing angular disparity. Therefore, reducing the angular disparity leads to a slight improvement in image contrast but at a cost in axial spatial resolution.

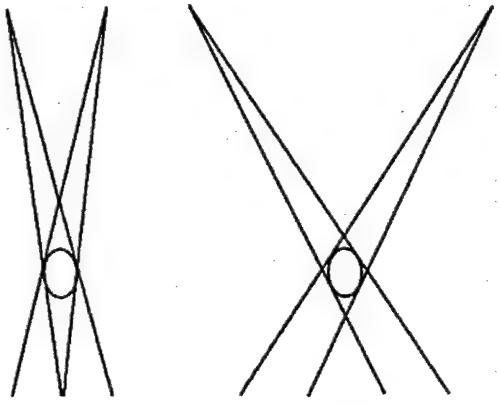

FIG. 4. Axial and in-plane spatial resolution vs angular disparity. Shown is how the amount of angular disparity affects the axial and in-plane spatial resolution. The diamond that superscribes the object defines the spatial resolution associated with ETACT. As the angular disparity is increased, the axial improves (the diamond is shorter), but the in-plane resolution worsens slightly (the diamond gets wider).

IV. DISCUSSION

ETACT has previously demonstrated the potential for the detection of small tumors in scintimammography.[5] However, the optimal manner in which to acquire clinical data has yet to be defined. In this investigation, we sought to determine the effect of angular disparity on image quality. Therefore, we evaluated its effect on image quality and axial spatial resolution. Reducing the angular disparity yielded an improvement in contrast at the cost of a degradation in axial spatial resolution. These results would appear to be contradictory. In most tomographic cases, improving spatial resolution yields an improvement in contrast. In SPECT, limited axial spatial resolution would typically indicate a thicker slice profile such that the activity associated with the tumor would be diluted by portions of the slice that do not contain the tumor. In Fig. 4, two cases with different angular disparities are illustrated. The small, round objects are noted as open circles. The angular disparity is noted by the distance between the two apertures at the top of Fig. 4, thus the configuration on the left has a smaller angular disparity than the one on the right. The spatial resolution is indicated by the diamonds that superscribe the two small, round objects. The vertical length of the diamond indicates the axial spatial resolution and the horizontal width indicates the in-plane spatial resolution. As can be seen, smaller angular disparity yields degraded axial spatial resolution (longer diamond) but better in-plane spatial resolution (thinner diamond) than does larger angular disparity. Therefore, the contrast degrades slightly with larger angular disparity due to a slight reduction in in-plane spatial resolution, even though the axial spatial resolution is improved.

For ETACT applied to scintimammography, the detection of small tumors is more important than the ability to localize the tumors axially. For this reason, the higher contrast associated with the smaller angular disparity would be considered more desirable than improved axial spatial resolution. Thus, one should lean toward smaller angular disparity. On the other hand, there was only a marginal difference in contrast between 10° and 15° angular disparity, and the improvement in axial spatial resolution was significant. Thus, an angular disparity of 15° is considered reasonable for this clinical application.

In summary, ETACT has shown the potential for the detection of small tumors in scintimammography. Using a smaller angular disparity between the acquired projections in ETACT was shown to lead to an improvement in image contrast but at a cost of degraded axial spatial resolution. The improvement in contrast is due to a slight improvement in the in-plane spatial resolution. Because improving the contrast leads to a subsequent improvement in the signal-to-noise ratio and thereby tumor detectability, one should lean toward using a smaller angular disparity. On the other hand, the difference in contrast between 10° and 15° was very slight and thus a 15° angular disparity is considered reasonable for clinical applications.

[a]Electronic mail: ffahey@wfubmc.edu

[1]B. Overmoyer, "Breast cancer screening," Med. Clin. North Am. **83**, 1443–1466 (1999).
[2]I. Khalkhali *et al.*, "Technetium-99m–sestamibi scintimammography of breast lesions: Clinical and pathological follow-up," J. Nucl. Med. **36**, 1784–1789 (1995).
[3]H. Palmedo *et al.*, "Scintimammography with Tc-99m MIBI in patients with suspicion of primary breast cancer," Nucl. Med. Biol. **23**, 681–684 (1996).
[4]J. F. Faumeni, Jr., R. N. Hoover, S. S. Devesa, and L. J. Kinlen, "Epidemiology of cancer," in *Cancer: Principles and Practice of Oncology*, 4th ed., edited by V. T. DeVita, S. Hellman, and S. A. Rosenberg (Lippincott, Philadelphia, 1993), pp. 150–181.
[5]F. H. Fahey, *et al.*, "Emission tuned-aperture computed tomography: A novel approach to scintimammography," J. Nucl. Med. **42**, 1121–1127 (2001).
[6]R. L. Webber, R. A. Horton, D. A. Tyndall, and J. B. Ludlow, "Tuned-aperture computed tomography (TACT). Theory and application for three-dimensional dento-alveolar imaging," Dentomaxillofac Radiol. **26**, 53–62 (1997).
[7]R. L. Webber and J. L. Hendrickson, "A comparison of the effect of task-specific with fixed beam alignment in tuned-aperture computed tomography," Dentomaxillofac Radiol. **29**, 223–229 (2000).
[8]R. L. Webber, H. R. Underhill, and R. I. Freimanis, "A controlled evaluation of tuned aperture computed tomography applied to digital spot mammography," J. Digit Imaging **13**, 90–97 (2000).
[9]R. A. Vogel, D. Kirch, M. LeFree, and P. Steele, "New method of multiplanar emission tomography using a 7-pinhole collimator and an Anger camera," J. Nucl. Med. **19**, 648–654 (1978).
[10]R. A. Vogel, D. L. Kirch, M. T. LeFree, J. O. Rainwater, P. P. Steele, "Tl-201 myocardial perfusion scintigraphy — results of standard and multi-pinhole tomographic techniques," Am. J. Cardiol. **43**, 787–793 (1979).
[11]H. R. Rizi, R. C. Kline, J. H. Thrall, M. C. Besozzi, J. W. Keyes, Jr., W. L. Rogers, J. Clare, and B. Pitt, "Tl-201 myocardial scintigraphy- a critical comparison of 7- pinhole tomography and conventional planar imaging," J. Nucl. Med. **22**, 493–499 (1981).
[12]M. T. LeFree, R. A. Vogel, D. L. Kirch, and P. P. Steele, "Seven-pinhole tomography- a technical description" J. Nucl. Med. **22**, 48–54 (1981).
[13]W. Chang, S. L. Lin, and R. E. Henkin, "A new collimator for cardiac tomography—the quadrant slant-hole collimator," J. Nucl. Med. **23**, 830–835 (1982).
[14]O. Ratib, E. Henze, E. Hoffman, M. E. Phelps, and H. R. Schelbert, "Performance of the rotating slant-hole collimator for the detection of myocardial perfusion abnormalities," J. Nucl. Med. **23**, 34–41 (1982).
[15]S. Dale and D. Bone, "Tomography using a rotating slant-hole collimator and a large number of projections," J. Nucl. Med. **31**, 1675–1681 (1990).
[16]P. F. Hemler, R. L. Webber, and F. H. Fahey, "Modeling and error identification of three dimensional tomosynthetic reconstructions," Proc. SPIE **3979**, 1280–1287 (2000).

Three-dimensional, tuned-aperture computed tomography reconstruction using hybrid imaging systems

Richard L. Webber, Stephen B. Robinson*, Frederic H. Fahey
Division of Radiologic Sciences and Department of Mathematics*, Wake Forest University, Winston-Salem, NC

Send correspondence to:

Frederic H. Fahey, D.Sc.
PET Center
Wake Forest University School of Medicine
Medical Center Blvd
Winston-Salem, NC, USA 27157
ffahey@wfubmc.edu

Abstract

A simple method has been developed that facilitates the production of spatially homologous three-dimensional (3D) reconstructions of radiographic data using Tuned-Aperture Computed Tomography® (TACT®). This is accomplished by acquiring the fiducial information essential for projection registration using a separate imaging device from that used for the data to be reconstructed. For example, an optical system rigidly attached to an x-ray source allows for direct inference of the underlying projection geometry associated with the x-ray beam and detector. This method does not require accurate knowledge of the position of the camera relative to the x-ray source in order to produce consistent, high-quality 3D reconstructions of the object. Correction for any scaling differences between the two modalities is also not required. We present the theoretical rationale for this approach as well as a preliminary phantom study. The mathematical treatment proves the validity of the approach and defines its geometric constraints. A tomographic phantom with external markings that were optically visible but radiolucent was imaged with a hybrid system that consisted of a digital camera rigidly mounted to a mammographic x-ray tube. Corresponding optical and x-ray projection images were acquired at four different angles relative to the phantom. The locations of the fiducial markers determined from the optical images were superimposed onto the corresponding radiographic images without prior calibration or scale correction. The accuracy of the TACT reconstruction performed using these fiducial locations was shown to be excellent and limited, in this experiment, by the method used to determine the position coordinates of the fiducial markers. In conclusion, a relatively inexpensive digital camera can be mounted to a projection-based x-ray machine to generate high-quality 3D radiographic images without prior calibration. The power of this approach is that every radiographic system can be easily converted into a tomographic system by the addition of a simple, digital camera without any complicated cross-calibration schemes.

1. Introduction

Tuned-Aperture Computed Tomography® (TACT®) is a new three-dimensional (3D) imaging technology that allows a 3D data set to be generated from multiple two-dimensional (2D) radiographic projections. (Webber 1997) Whereas most other projection-based methods for generating 3D data require a stable or rigid projection scheme, these projections can be taken from completely random angles and positions. The fact that TACT can accommodate 2D images produced from random or even unknown projection angles is important because it greatly simplifies the reconstruction process and produces accurate and precise 3D images having properties that can be custom tailored to a large variety of diagnostic uses. Such advantages are particularly important for biomedical applications because inevitable patient motion and concerns for mitigating dose ultimately limit task-dependent sampling strategies. TACT has been successfully applied to a variety of medical imaging applications including dentistry, mammography and nuclear medicine. (Webber 1994, Webber 1997A, Webber 2000, Fahey 2001)

However, these potential advantages come at the cost of inferring the underlying 3D-projection geometry from fiduciary measurements obtainable from each 2D component projection. A minimum number of fiducial relationships must be obtained for 3D reconstruction depending on the number of degrees of freedom underlying the sampling geometry used to produce the original projections. (Webber 1997B, Webber 2001) This required information may be determined from the projected positions of a set of fiducial point markers strategically placed about the object and visible on all of the acquired projections. These markers may be intrinsic, anatomical details that can be recognized individually in each projection, but more commonly are extrinsic markers attached to the object near the region of diagnostic interest with high contrast and hence, are easily recognizable in each projection. We have shown previously that it is possible to reconstruct 3D images unequivocally from any spatially unconstrained series of individual projections provided each contains up to six appropriately distributed and individually recognizable reference points. (Webber 1997B, Webber 2001) However, when these many points are extrinsically attached to the object, they may introduce

significant problems with image interpretation. Since they must be identifiable on all projections, they may obscure certain regions of potential diagnostic interest on at least some of the projections. Conversely, if they overlie a region of signal density comparable to their own, it may be very difficult to localize them, thus precluding their required localization in all projections.

This report describes a new approach that eliminates both of these basic shortcomings through hybrid imaging; that is, the use of two separate but spatially coupled imaging modalities, one for acquiring the tomographic data and the other for acquiring the fiducial information. For example, a conventional digital photographic camera can be coupled to a digital x-ray system in such a way that it photographs fiducial patterns that are highly visible but radiolucent and are fastened to the object near the region of diagnostic interest. Since the patterns are radiolucent, the difficulty in isolating the fiducial information from the radiograph is eliminated. The only information required from the resulting photographic images is the precise recording of the fiducial information. High-resolution photographic images of the fiducial patterns can be efficiently produced with very high signal-to-noise ratios. This greatly simplifies the challenge of developing software to automatically track and process projection information essential for accurate 3D reconstruction using the TACT algorithm. (Webber 1994, Webber 1997B, Webber 1999) The image data must be acquired in a synchronized fashion such that each projection is represented by an image pair, one photographic and one radiographic. This constraint assures that the photographs of the fiducial patterns can be appropriately converted into the information required to reconstruct the underlying radiographic projections into a unified 3D x-ray image. Beyond a few other geometric constraints that will be specified, no calibration need be performed to generate a consistent 3D x-ray image. The exact geometric relationship between the two imaging modalities need not be known and no correction need be applied for the difference in scaling between the two systems. We present a mathematical treatment in the next section that discusses the geometric rationale underlying this scheme defining the geometric constraints necessary to lead to the reconstruction of a consistent data set. This is followed by a preliminary phantom experiment that demonstrates the feasibility of the concept.

2. Theoretical Rationale

In this section we provide a mathematical foundation for our experimental work. We begin by introducing the notation and terminology that allows a precise statement of the reconstruction problem. An important first step is to define what it means to obtain a *usable back-projection scheme* based upon the camera's point-of-view rather than the x-ray source's point-of-view. We then present a general theorem describing how the set of camera positions must be related to the corresponding set of source positions in order to achieve a usable back-projection scheme. We illustrate the theorem with several examples, one of which corresponds to the projection geometry assumed during our phantom study. Finally, it is reasonable to expect that our reconstruction will distort some aspects of the original object. We provide a detailed discussion that shows that this distortion is not serious. In fact, horizontal slices of the original object transform to horizontal slices of the reconstructed object, and the transformation between these slices involves only a rescaling and a shift. Hence all features in a reconstructed slice are similar to those in the corresponding original slice and important features in the original object will still be easily recognizable in the reconstruction.

2.1 Definitions

Assume that n x-ray images are created. To back-project each image in the standard way we must discover the relative positions of the x-ray source, the object, and the image plane for each image. In all that follows we assume that the image plane is the $x-y$ plane in standard Euclidean space, $\Re^3$, and that all measurements are made relative to this frame of reference. Further, by previous work we know that we can assume, without loss of generality, that the patient maintains a fixed position relative to the image plane as the images are created. Webber *et al.* described how images created with uncoupled image plane, patient and source can be transformed to this simpler case. (Webber 1997A)

Let $P := \{p_1, p_2, ..., p_n\}$ represent the positions, in $\Re^3$, of the x-ray source during the creation of the n images. The corresponding set of camera positions is represented by $P' := \{p'_1, p'_2, ..., p'_n\}$. Given an arbitrary point, x, in the object, we will refer to the associated image points, that is the projection of x by $\{p_1, p_2, ..., p_n\}$, as $\{u_1, u_2, ..., u_n\}$. Of course, each u_j is simply the intersection of the line $\overleftrightarrow{p_j x}$ with the $x-y$ plane, and it is clear that the lines $\overleftrightarrow{p_1 u_1}, \overleftrightarrow{p_2 u_2}, ..., \overleftrightarrow{p_n u_n}$ are concurrent at the point x. This configuration is shown in Figure 1. Our alternative back-projection scheme must correlate the image data in a similar way with p_i' substituted for p_i. This motivates the following definition.

Definition: P' provides a *usable back-projection scheme* relative to P if and only if, given any point, x, and its associated image points, $\{u_1, u_2, ..., u_n\}$, then the lines $\overleftrightarrow{p'_1 u_1}, \overleftrightarrow{p'_2 u_2}, ..., \overleftrightarrow{p'_n u_n}$ are concurrent at a point x'.

The central theoretical problem can now be stated as: *Given a set of source points, P, find a geometric characterization of the associated set of camera points, P', such that P' provides a usable back-projection scheme relative to P.*

In order to state the upcoming theorems in their broadest sense we must allow the concept that parallel lines meet at a point at infinity, and thus any two coplanar lines must intersect. This approach is common in projective geometry and allows a more unified presentation of ideas. We will see in later discussion that this does more than simply allow an interesting abstraction. In fact, the primary practical applications of our theoretical statements, including our experimental data, involve exactly these geometric situations.

Theorem: P' provides a usable back-projection scheme relative to P if and only if P and P' are perspective with respect to the image plane, i.e. if and only if given any $1 \le i < j \le n$ the corresponding lines $\overleftrightarrow{p_i p_j}$ and $\overleftrightarrow{p'_i p'_j}$ intersect at a point on the image plane.

The proof of this theorem is included in the appendix. Two corollaries follow quickly from this theorem. The first gives an additional criterion for visualizing the sets P and P', and the second verifies that an appropriate geometry was used during our data collection.

Corollary 1: If P' provides a usable back-projection scheme relative to P, then P and P' are perspective with respect to a point, i.e. the lines $\overrightarrow{p_1p_1'}, \overrightarrow{p_2p_2'}, \ldots, \overrightarrow{p_np_n'}$ intersect at a point q.

Remark: It is important to notice that it is necessary, but not sufficient, that the set of source points and the set of camera points be perspective with respect to a point.

Corollary 2: If P and P' describe similar polygons with parallel edges where both polygons are horizontal with respect to the image plane, then P' provides a usable back-projection scheme relative to P.

Remark: If the corresponding edges of the two polygons are parallel, then it immediately follows that the polygons are similar.

2.2 Evaluating Distortion in the Reconstruction

In this section we assume that P' provides a usable back projection scheme relative to P, and we investigate the relationship between the original object, which would ideally be located via the back-projection associated with P, and the reconstruction using the back-projection scheme associated with P'. We will see that a horizontal slice of the original object must correspond to a horizontal slice of the reconstructed object, although possibly at a different height. Moreover, the transformation from the actual slice to the reconstructed slice will include only a rescaling and a shift, i.e. a similarity. Thus objects in an actual slice will be transformed to similar objects in the reconstructed slice, and will be clearly recognizable. The following theorem provides the details for both of the above statements.

Theorem: Suppose that P' provides a usable back projection scheme relative to P, and that $x=(x,y,z)$ and $x'=(x',y',z')$ are corresponding points in the original object and its reconstruction, respectively. Then there are constants $k, h,$ and h', which depend only on P' and P, such that $\frac{z'}{h'-z'}=k\frac{z}{h-z}$. (Typically, h and h' will represent the heights of selected points in P' and P.) Moreover, there is a shift vector, s, and a scaling factor, λ, which depend only on P', P, z, and z', such that $x'=\lambda x+s$.

The proof of this theorem is included in the appendix. This relationship simplifies considerably when we consider special cases. For example, if P and P' represent parallel congruent polygons in a horizontal plane at height h, as in our data collection, then we deduce that $z=z'$ and $x'=x+\frac{z}{h}(p_2'-p_2)$.

2.3 Assuming an Affine Projection Geometry

In many applications it is reasonable to assume that the x-rays passing through the object are parallel. This *affine* geometry makes sense, for example, when the source-to-image distance is large relative to the object-to-image distance. Assuming an affine geometry introduces several significant simplifications. First, at most four fiducial reference points are needed to process the image data even when the source, the object, and the image detector are completely uncoupled. When the patient and the image plane are rigidly attached, then only one reference point is needed.

All of the results in the previous sections can be adapted to this simpler situation. We state these adapted results without proof. Note that the sets P and P' now represent points at infinity, or they can be represented as sets of direction vectors $p=(p_1,p_2,h)$. The constant height h is arbitrary, but $h=1$ is a convenient.

Theorem: P' provides a usable back-projection scheme relative to P if and only if P and P' are similar polygons with parallel corresponding edges.

For this situation the TACT algorithm is at its simplest. The image of a single fiducial reference point, x, will be a set $U = \{u_1,...,u_n\}$, which must describe a polygon similar to both P and P'. To perform the reconstruction of a slice let c represent any point in the plane, shift all of the images by proportional amounts towards c, and then average the results. Notice that if the set U, and its center of gravity are shifted by any amount in the image plane, then the reconstruction algorithm will still work since the shifted U simply represents the image of a horizontally shifted fiducial reference point. The slices of the first reconstruction will exactly correspond to slices of the second reconstruction as long as the shifts towards the arbitrarily chosen point are proportional. Similarly, if we shrink or stretch U to create a similar polygon, then the reconstruction will still be valid, since the rescaled U now represents the image of a fiducial reference at a different height. Moreover, the original reconstruction slices and the new reconstruction slices will be identical as long as the shifts towards c are equal.

3. Methods

We performed a simple phantom experiment to demonstrate the feasibility of the technique and to illustrate how this approach may be applied in a simulated, clinical setting. A tomographic phantom was fixed to the imaging plane. This phantom consists of 12 radiopaque, numeric characters (integers) imbedded in plastic at different heights. Each number is 1 mm thick and the center-to-center spacing between the numbers is approximately 1 mm. The x-ray source was constrained to move in an arc above the image plane, and a photographic, digital camera (Sony Cyber-Shot DSC-P1) was rigidly attached to the x-ray source from a digital mammographic device (Instrumentarium Alpha IQ Delta 16) such that the vector representing the displacement difference between the x-ray source and the camera remained fixed. A photograph as well as a schematic

illustrating this configuration are shown in Figure 2. The level of the lens of the digital camera was adjusted so that its vertical distance from the x-ray detector was 60 cm and was within a centimeter of being the same as the focal spot of the x-ray tube. It was approximately 40 cm from the top of the phantom to the x-ray focal spot. The distance between the x-ray focal spot and the lens of the digital camera was unknown. The camera was oriented so that the complete region of interest on the x-ray table could be photographed without obstruction by the collimating apparatus attached to the x-ray tube. A photograph of the phantom is shown in Figure 3A. A piece of paper with 4 markers drawn on it was fixed to the top of the phantom such that these markers were coplanar to the imaging plane. Two additional visible markers were placed 7.5 cm above the phantom. Only one of these markers was used in the TACT reconstruction process, the other intended for future investigations.

The projection geometry requires that the angle assumed by the photographic camera relative to the object be unchanged from one projection to the next. The phantom was imaged from multiple angles using a digital, mammographic unit. This constraint is clearly not met when the camera is fastened rigidly to a tilting tube head as shown in Figure 2. One solution to this problem would be to "level" the camera physically between projections. However, the same can be realized analytically by means of a projective transformation of the resultant photographs. We chose this alternative because of its advantages for simple adaptation to existing x-ray equipment. This projective correction entailed mapping the four coplanar markers seen on all the photographs of the phantom into those positions that were seen by the camera at some reference position. This reference position was chosen to be when the camera was directly above the phantom. This correction was accomplished prior to determining the relative displacements of a fifth marker located above the phantom that was used by the TACT reconstruction algorithm for establishing respective tomosynthetic shifts required for proper back-projection. It should also be noted that the x-ray source moved in an arc and thus was not always constrained to the same plane as prescribed by the theory. However, in this experiment, the source traveled on 15^{o} from vertical and the potential amount of distortion introduced was predicted to be a small fraction of a millimeter, and thus considered to be inconsequential from a practical sense.

No attempt was made to directly measure the projection geometry of the system. All of the required 3D information was inferred from the associated photographic images of the fiducial markers as seen by the digital camera. These images were paired with projection radiographs produced at 4 arbitrarily selected angles measured parallel to the constrained linear motion of the x-ray source and perpendicular to imaging plane: -15°, -10°,-5°, 0°. A representative photograph/radiograph pair is shown in Figures 3, after selective cropping to restrict their extents to the region of interest. The location of one of the fiducial markers was noted on each of the 4 photographic images. These locations were transferred to the corresponding radiographic images without correcting for the difference in scale between the two sets of images. The data were reconstructed using the TACT method with these marker locations to determine the appropriate amount to shift each projection prior to addition. In other words, the radiographic projection data were back-projected using the transferred photographic marker locations and no information inherent to the radiographs themselves. The resulting 3D reconstructions (tomographic slices) were checked for registration precision and inter-slice linearity. By noting the observed distances between optimally converged reconstructions of the sequentially distributed radiopaque integers in the phantom and comparing them with the known spacing allowed us to check the inter-slice linearity of the reconstructions.

4. Results

Figure 4 shows a selection of back-projected slices through the phantom using reconstruction parameters determined exclusively from the photographic images. The fact that the integers ("1" in Figure 4A) appear to be in proper focus when a fixed inter-slice distance was selected for reconstruction assures that the observed distance between the integers is proportional to the actual fixed distance built into the phantom. Note also the high degree of spatial convergence associated with the reconstructed planes containing each individual test integer. This demonstrates that the locations required by the TACT reconstruction algorithm can be appropriately inferred from the photographic data. An even more stringent demonstration of the registration accuracy resulting from this hybrid

method is shown in Figure 4B. In this figure, isolated particulate debris located on the surface of the tomographic phantom is clearly imaged. The clarity of the reconstruction of these tiny particles demonstrates a level of precision that approaches the resolution limit of the interactive system we used to visually identify the respective positions of the fiducial markers.

No information inherent to the series of radiographs was incorporated into the reconstruction process. Only information from the corresponding photographic images was used. These data clearly demonstrate that the TACT algorithm can use information derived from a second (radiolucent) modality to produce linearly 3D reconstructions from radiographic projections. No cross-calibration between the modalities or correction for scale differences was necessary to generate a completely consistent, tightly converged, and linearly distributed set of reconstructed slices. In addition, it was not necessary to know the distance between the focal spot of the x-ray tube and the lens of the digital camera. In this experiment the only required geometric constraints were that the digital camera be fixed to the x-ray tube such that the displacement vector between the two is constant, the optical markers be fixed to the phantom, and the phantom be fixed to the x-ray detector.

5. Discussion

We have demonstrated the potential for using hybrid imaging information to produce high quality, spatially homologous TACT reconstructions. This greatly simplifies the data acquisition process for TACT. Any radiographic system can be converted into a tomographic device by simply mounting a digital camera to the system and applying some visible external markers to the object. The reconstruction software is simple and can be easily implemented on a standard personal computer. This approach is not only simple but it eliminates the ambiguity that is sometimes introduced into the TACT reconstruction process by the overlying of radiopaque markers onto features of diagnostic interest. The radiopaque markers previously necessary for TACT are now

replaced with markers that need only be visible when viewed in digital photographs acquired simultaneously to the radiographic projections. This simplification of the TACT method substantially widens the range of clinical applications to which it can potentially be applied.

Our mathematical treatment indicates that fiducial data acquired from an offset system can be appropriately applied during the back-projection process without specific knowledge as to the geometric relationship between these two devices. Therefore, no cross-calibration to describe either the geometric relationship or scaling differences between the two systems is required. Although these data are reconstructed consistently without cross-calibration or scale correction, it is not possible to determine the absolute location of a particular slice. As noted in the mathematical treatment, even if the data are scaled correctly, the back-projection will be consistent but will not correspond to the same back-projected point in the photographic image set and may even be in a different parallel plane. Although we attempted to keep the lens of the digital camera in the same plane as the x-ray focal spot, if we did not succeed, then we will be reconstructing slightly different planes.

In addition, if we do not correct for scale differences between the two data sets, the set of projected marker locations will define polygons that are similar but of different sizes. This will also lead to the reconstruction of different planes. In conventional TACT, adding the projection data without shifting reconstructs the image plane. Shifting the data such that the locations of the fiducial markers align, leads to the reconstruction of the plane that contains the fiducial marker and is parallel to the image plane. Shifting the projection data a set fraction of the amount necessary to align the projections of the fiducial marker, reconstructs a plane that is parallel to the image plane and is that fraction of the distance between the image plane and plane containing the fiducial marker. For example, shifting 1/3 of the distance will reconstruct the plane that is parallel to the image plane and is 1/3 of the distance between the image plane and the fiducial marker. If the polygon resulting from the marker projections in the photographic data is similar but smaller than that for the radiographic data, then the data will also be shifted a set fraction of the distance necessary for the reconstruction of a particular plane in the

radiographic data set. Therefore, the resultant reconstructed plane will be parallel to this plane but will be closer to the image plane.

In many clinical applications where tomography may be applied, the highly consistent 3D reconstructions provided by this approach are more than adequate and absolute knowledge of the exact location of a particular slice typically is not necessary. For example, tomography may allow the breast imaging specialist to determine that the microcalcifications seen on the 3D mammogram align along a blood vessel and thereby aid in the diagnosis whereas the exact distance those microcalcifications lie above the image plane may not be particularly useful. Therefore, 3D radiographic data of clinical import can be obtained using the approach described without any cross-calibration or scale correction between the photographic and radiographic systems. However, we are currently investigating the use of a simple calibration scheme that will allow accurate localization of the reconstructed slices as well as correcting for the fact that the acquired projections are not affine as is inherently assumed in the reconstruction process.

In conclusion, we have developed a simple scheme that uses a hybrid imaging system consisting of digital photography and radiographic systems to acquire the fiducial information and projection data, respectively. We have presented a mathematical treatment that indicates that highly consistent reconstructions can be generated from these data without any cross-calibration or scale corrections between the two systems. There are some simple geometric constraints presented in this treatment that can be easily implemented in a clinical environment. We presented the results of a preliminary phantom experiment that demonstrated the feasibility of the approach and how it may be applied in a clinical environment. This approach to TACT provides an extremely simple method of 3D radiographic such that any radiographic unit could be easily converted into a tomographic device.

6. Appendix

Theorem: P' provides a usable back-projection scheme relative to P if and only if P and P' are perspective with respect to the image plane, i.e. if and only if given any $1 \le i < j \le n$ the corresponding lines $\overleftrightarrow{p_i p_j}$ and $\overleftrightarrow{p'_i p'_j}$ intersect at a point on the image plane.

Proof: Suppose that P' provides a usable back-projection scheme relative to P. Let $1 \le i < j \le n$. Let x and x' represent an arbitrary point and its back-projection, as described above. Since the lines $\overleftrightarrow{p_i u_i}$ and $\overleftrightarrow{p_j u_j}$ intersect at the point x, then the points p_i, p_j, u_i, u_j must be coplanar, and similarly for the points pi', pj', ui, uj. These two planes intersect along the line $\overleftrightarrow{u_i u_j}$. Since they are coplanar the lines $\overleftrightarrow{p_i p_j}$ and $\overleftrightarrow{u_i u_j}$ will meet at some point c in the $x-y$ plane, and similarly the lines $\overleftrightarrow{p'_i p'_j}$ and $\overleftrightarrow{u_i u_j}$ will meet at some point c'. Notice that c and c' are independent of the choice of x, since they are determined by the intersections of the lines $\overleftrightarrow{p_i p_j}$ and $\overleftrightarrow{p'_i p'_j}$ with the image plane. However, $\overleftrightarrow{u_i u_j}$ contains both c and c', and since this line changes as x changes, it must be that $c = c'$ and that the lines $\overleftrightarrow{u_i u_j}$ pivot around c as x changes. Hence, the lines $\overleftrightarrow{p_i p_j}$ and $\overleftrightarrow{p'_i p'_j}$ intersect at a common point on the image plane.

Conversely, if the line $\overleftrightarrow{p_i p_j}$ meets the line $\overleftrightarrow{p'_i p'_j}$ at a point c in the image plane, then the projections of any x onto points u_i, u_j will imply that the points p'_i, p'_j, u_i, u_j lie in the plane spanned by the lines $\overleftrightarrow{u_i u_j}$ and $\overleftrightarrow{p'_i p'_j}$. Thus the lines $\overleftrightarrow{p'_i u_i}$ and $\overleftrightarrow{p'_j u_j}$ are in a common plane and must meet at a point x'. This argument works for all pairings with $1 \le i < j \le n$, so all such lines are concurrent in pairs. It follows that $\overleftrightarrow{p'_1 u_1}, \overleftrightarrow{p'_2 u_2}, \ldots, \overleftrightarrow{p'_n u_n}$ are all concurrent at the point x'.

Q.E.D.

Theorem: Suppose that P' provides a usable back projection scheme relative to P, and that $x=(x,y,z)$ and $x'=(x',y',z')$ are corresponding points in the original object and its reconstruction, respectively. Then there are constants $k,h,$ and h', which depend only on P' and P, such that $\frac{z'}{h'-z'}=k\frac{z}{h-z}$. (Typically, h and h' will represent the heights of selected points in P' and P.) Moreover, there is a shift vector, s, and a scaling factor, λ, which depend only on P', P, z, and z', such that $x'=\lambda x+s$.

Proof : First consider the point $x=(x,y,z)$ in the original object, which the sources p_1 and p_2 project onto the points u_1 and u_2. Without loss of generality, p_2 lies on or above the horizontal plane containing p_1. For the purposes of this discussion we assume that it is strictly higher because this represents the more difficult case. Let $\overline{p}_1$ represent the intersection of the line $\overleftrightarrow{p_1u_1}$ with the horizontal plane containing p_2, and let h represent the height of this plane. Then a simple application of similar triangles shows that

$\frac{\|u_2-u_1\|}{\|p_2-\overline{p}_1\|}=\frac{z}{h-z}$ and $\frac{\|u_1-c\|}{\|p_2-\overline{p}_1\|}=\frac{p_{13}}{h-p_{13}}$ where p_{13} represents the third component of p_1. These formulae combine to give $\frac{z}{h-z}=\frac{\|u_2-u_1\|}{\|u_1-c\|}\frac{p_{13}}{h-p_{13}}$.

A similar formula holds for the height of the reconstructed point x' and we deduce the relationship $\frac{z'}{h'-z'}=\left[\frac{p'_{13}}{p_{13}}\frac{h-p_{13}}{h'-p'_{13}}\right]\frac{z}{h-z}$. This describes a 1-1 correspondence between z and z', and the expression in brackets depends only on the properties of P and P'.

In the case that p_1 and p_2 are at the same height, our theorem implies that p_1'and p_2' describe a segment that is parallel to $\overleftrightarrow{p_1p_2}$, but possibly at a different height. The

intersection point, c, is now *at infinity*, so the previous derivation is no longer valid, but a straightforward similar triangles argument yields $\frac{z'}{h'-z'} = \left[\frac{\| p_2 - p_1 \|}{\| p'_2 - p'_1 \|}\right] \frac{z}{h-z}$.

Now hold z and z' constant and focus on the transformation of one horizontal slice to another. To describe this transformation we only need to follow the line from p_2 through an arbitrary point x in the plane at height z, find the coordinates of its image point u, and then follow the line $\overleftrightarrow{up'_2}$ until it crosses the plane at the height z'. A precise formula for this transformation is $x' = \left(\frac{h'-z'}{h'}\right)\left(\frac{h}{h-z}\right)x - \left(\frac{h'-z'}{z'}\right)\left(\frac{z}{h-z}\right)p_2 + \left(\frac{z'}{h'}\right)p'_2$, and we have verified the existence of an s and a λ with the desired properties.

QED

Acknowledgements

The authors would like to thank Endia Warren for her assistance in the acquisition of the phantom data. This work was supported by NIH R01 DE12227, DAMD 17-98-1-8349 and Instrumentarium Imaging.

References

Fahey F H, Grow K L, Webber R L et al. 2001 J Nucl Med **42** 1121-1127

Webber R L, inventor. Wake Forest University, assignee. 1994 Self-calibrated tomosynthetic, radiographic imaging systems, method and device. US Patent 5, 359, 637

Webber R L, Horton R A, Tyndall D A, Ludlow J B 1997A Dentomaxillofac Radiol **26** 53-62

Webber R L, inventor. Wake Forest University, assignee. 1997B Self-calibrated tomosynthetic, radiographic imaging systems, method and device. US Patent 5, 668, 844

Webber RL, Betterman W. 1999 Dentomaxillofac Radiol **28** 305-310

Webber R L, Hendrickson J L 2000 Dentomaxillofac Radiol **29** 223-229

Webber R L, Horton R A, inventors. Wake Forest University, assignee. 2001 Method and system for creating three-dimensional images using tomosynthesis computed tomography. US patent 6,289,235

Figure Captions

Figure 1. Geometric Configuration. Consider 3 x-ray source points P := p1,p2,p3 and an arbitrary source point within the object, x. Also note 3 camera position, P' :=p1',p2',p3', that correspond to P. The projection of x onto the image plane by the x-ray source points yields U := u1,u2,u3. If we back-project from U to 3 camera positions, P', and they all pass through a common point x', this is considered to be a usable back-projection scheme.

Figure 2. Photograph and Schematic of Experimental Configuration. The tomographic phantom is placed flat upon the digital detector. The source to detector distance is 60 cm. The digital camera is rigidly mounted to the x-ray tube and is placed at a slight angle such that the entire phantom with fiducial markers can be imaged in each projection.

Figure 3. Hybrid Image Pair. A. The photograph of the phantom with markers. A piece of paper with 4 markers was placed on the top surface of the phantom such that these are coplanar and parallel to the imaging plane. These coplanar markers were used to apply a projective transformation to the photographic data to correct for the fact that they were acquired at varying, slight angles relative to the image plane. Two additional markers are placed 7.5 cm above the phantom. One of these two was used during the TACT reconstruction process. B. Corresponding radiograph. The markers in A are totally radiolucent, and thus are not visible on the radiograph. Each radiopaque number is located on a different height above the imaging plane. The center-to-center distance between the letters is approximately 1 mm.

Figure 4. Selected Reconstructed Images. A. The plane though integer "1." B. The plane through the flat surface of the phantom showing highly resolved particulate debris indicating the quality the resultant reconstruction.

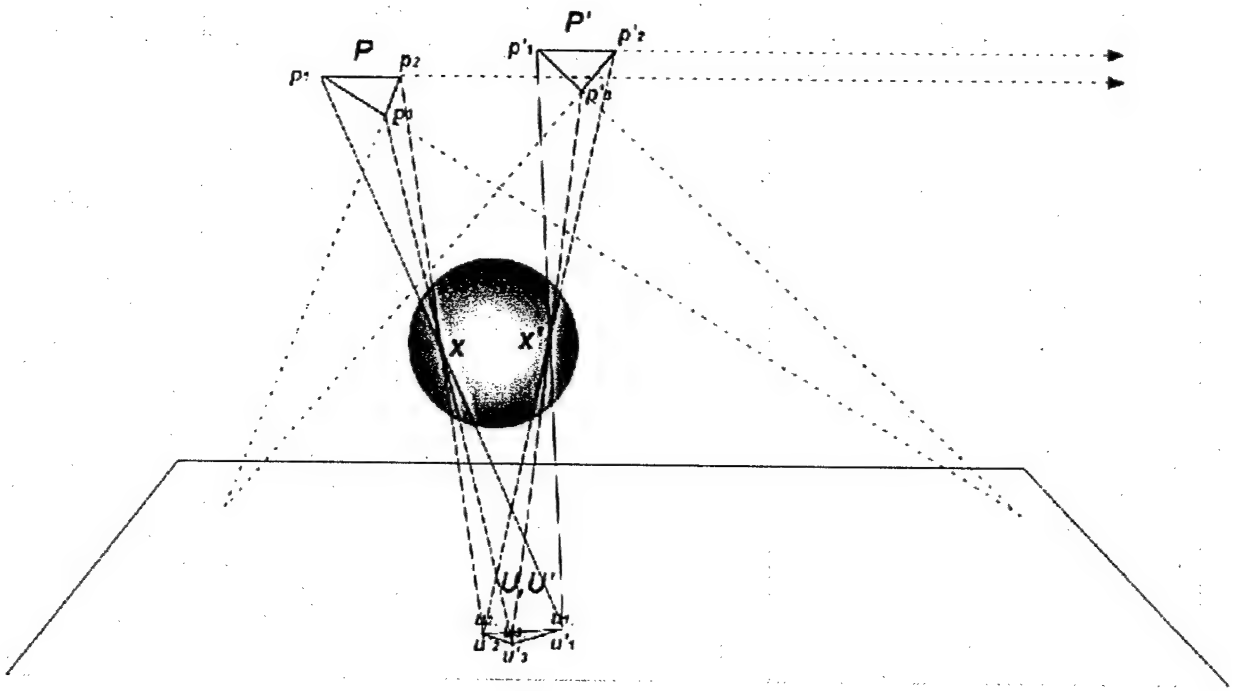
P
P'
X
X'
U,U'

Photograph

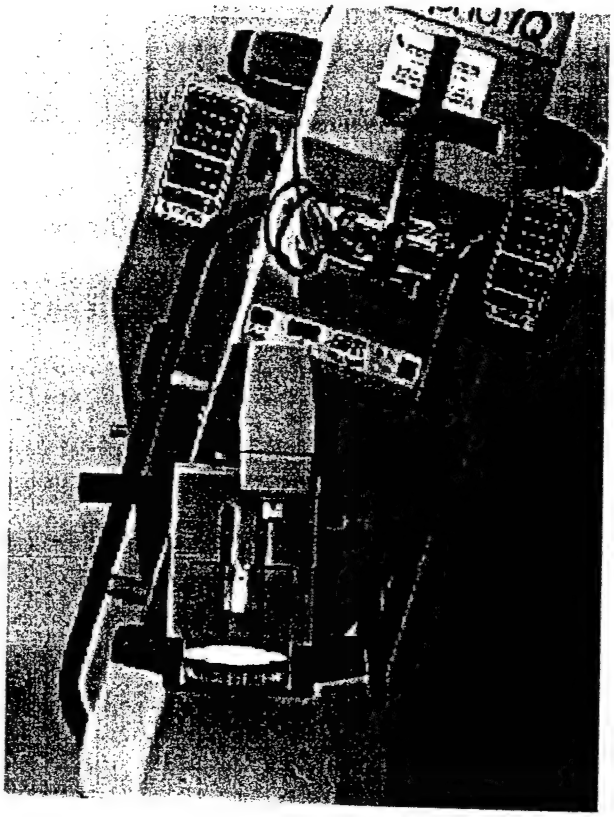

Schematic Diagram

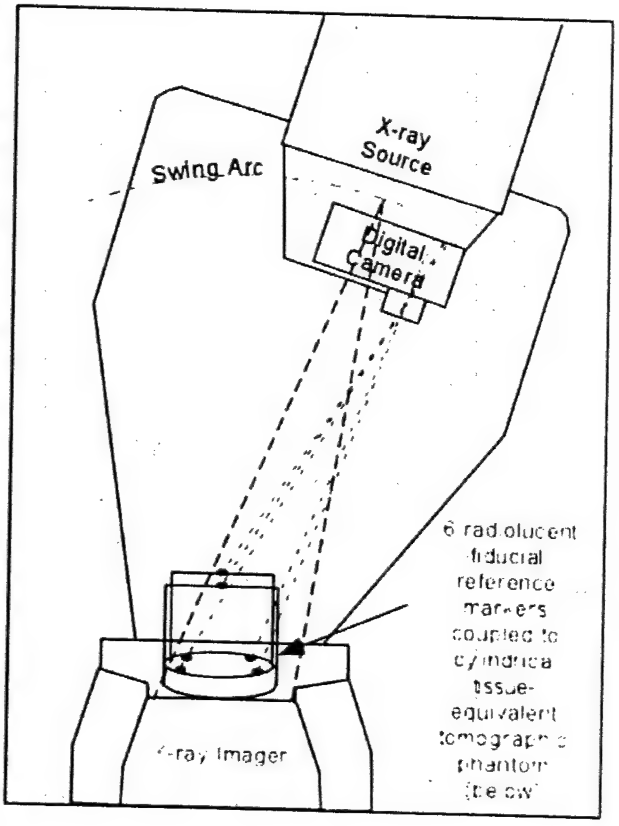

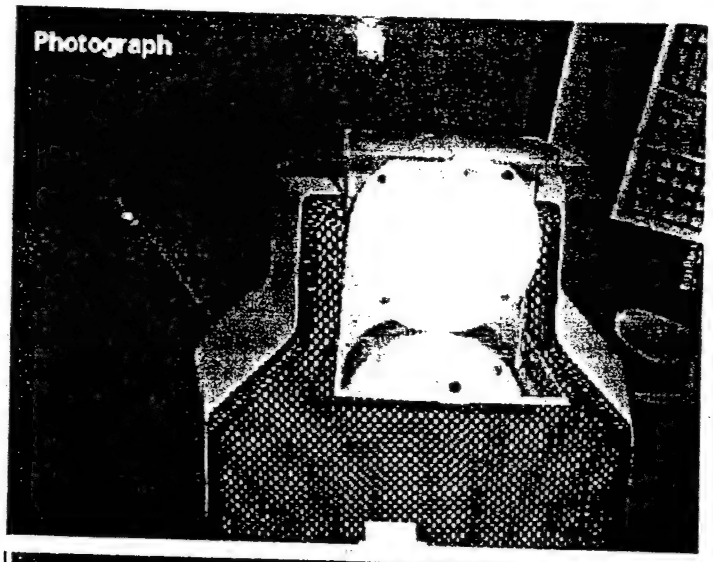
Photograph

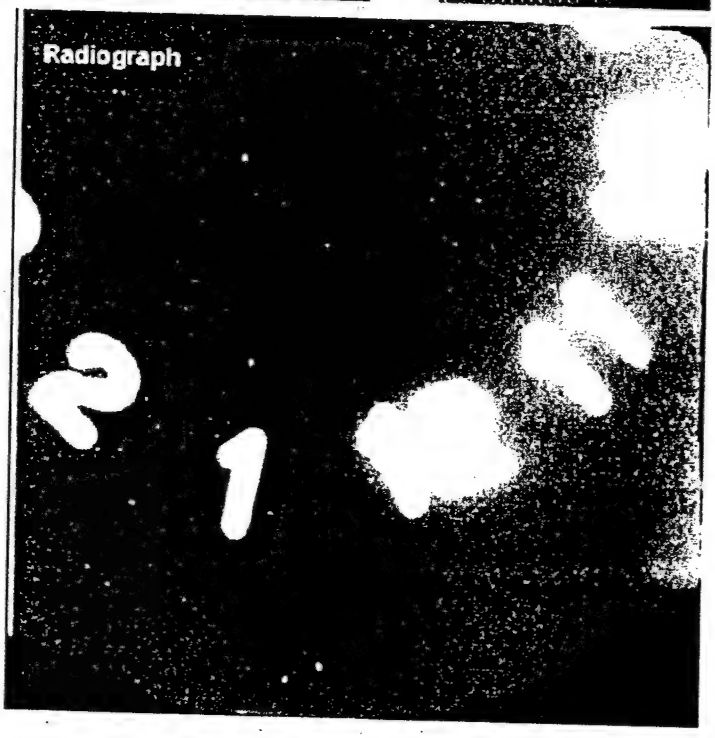
Radiograph
2
1

A
3
2
1

Submitted to Med Phys

Tuned-Aperture Computed Tomography

Paul F. Hemler[1], Stephen B. Robinson[2], Richard L. Webber[3], Fred Fahey[4]

[1]Department of Computer Science, Wake Forest University, Winston-Salem, NC, 27109
[2]Department of Mathematics, Wake Forest University, Winston-Salem, NC 27109
[3]Department of Dentistry, Wake Forest University School of Medicine, Winston-Salem, NC, 27157
[4]Department of Radiology, Wake Forest University School of Medicine, Winston-Salem, NC, 27157

Abstract:

This paper describes a unique system for constructing a three-dimensional volume from a set of two-dimensional (2D) x-ray projection images based on optical aperture theory. This proprietary system known as Tuned-Aperture Computed Tomography (TACT) is novel in that only a small number of projections acquired from arbitrary or task-specific projection angles is required for the reconstruction process. We used TACT to reconstruct a simulated phantom from seven 2D projections made with the x-ray source positioned within 30 degrees of perpendicular to a detector array. The distance from the x-ray source was also varied to change the amount of perspective distortion in each projection. Finally, we determined the reconstruction accuracy of TACT and compared it to that of a conventional tomosynthesis system. We found the reconstructed volumetric data sets computed with TACT to be geometrically accurate and contain significantly less visible blurring than a similar data set computed with the control technique.

Keywords: tomosynthesis, tuned-aperture computed tomography, TACT, limited angle tomography, cone beam.

1 Introduction

Tuned-Aperture Computed Tomography (TACT)[1] is a task specific three-dimensional (3D) imaging and reconstruction technique. TACT reconstructs a 3D volume from a set of two-dimensional (2D) x-ray projection images. The difference between TACT and other transmission radiographic systems is that the 2D images used in the reconstruction process are acquired without geometrical constraints. Specifically, the relationship between the x-ray source, object, and detector array is not fixed as in conventional computed tomography (CT), C-arm, tomosynthesis, and cone-beam systems. Geometry-free imaging holds the promise of generating accurate 3D volumetric image sets in a variety of situations that currently use 2D x-ray projection images.

TACT is a generalization of tomosynthesis, which refers to a variety simple reconstruction techniques that compute a 3D volumetric image representation from multiple 2D projections of an object [2, 3, 4, 5, 6, 7]. A renewed interest in tomosynthesis for medical and other applications, such as non-destructive testing has been spurred in recent years by the advent of 2D solid-state digital imagers.

TACT and tomosynthesis are distinct from CT in that tomosynthetic volumes can be reconstructed from a small number of projections (typically fewer than 20) and the projection angles are restricted (usually less than 30 degrees from perpendicular), leading to a finite imaging aperture. In CT, volume images are reconstructed from many projections (typically greater than 1000) and the projection angle is 90 degrees, leading to an infinite imaging aperture. The imaging aperture for these different systems is shown schematically in Figure 1.

Reconstructions arising from data sampled from finite imaging apertures as exemplified in Figure 1 by TACT and circular tomosynthesis, necessarily produce undersampled volume

representations. When reconstruction methods based on continuous geometric approximations are applied to such restricted data sets, they tend to produce significant inaccuracies. More specifically, reconstructions based on the Radon transformation usually are unusable because the resulting anisotropic projection samples associated with finite apertures usually lead to a poor approximation of the transformation integral. Fourier-transform based reconstruction methods also fail when an insufficient number of frequency-domain samples is acquired[8].

Because reconstruction methods based on isotropic approximations are not applicable to tomosynthesis and TACT, other methods characterized by varying amounts of spatial cross-correlation are employed. These reconstruction techniques use some form of the backprojection algorithm to approximate the imaged volume. The basic idea is to smear each projection through the reconstructed volume along the same path from which the respective projection was acquired. Therefore, the projection imaging geometry must be known prior to reconstruction for the backprojection to accurately reconstruct a volume [9, 10]. In tomosynthesis this imaging geometry is fixed and known prior to exposure, whereas in TACT the imaging geometry may not be fixed and/or may be unknown prior to exposure. To overcome the unknown and non-fixed imaging geometry reconstruction requirement, TACT incorporates a set of up to six fiducial markers that are purposely made visible in each projection image. These fiducials are used to compute the imaging geometry [11] for each projection. Once the imaging geometry is known, an extension of the standard tomosynthesis reconstruction method can be employed.

This paper presents a mathematical foundation for computing the unknown imaging geometry in the general case (no orientation or location restrictions other than complete representation by a perspective projection matrix). It incorporates a geometric interpretation of this matrix formulation, an implementation, and test results. Additionally, we compare

the tomosynthetic volume generated with TACT to a volume generated with a conventional tomosynthesis reconstruction method using the same set of 2D projection images. The geometric accuracy of the TACT system is verified experimentally on a simulated phantom. Finally, visually obvious differences in the 3D image of the phantom produced using TACT are noted relative to a control image generated tomosynthetically. Basic theories for determining any projection-based imaging geometry from multiple fiducial points are presented in [12, 13]. The underlying derivations are restated here in a more restricted context designed to make the derivations more tractable and obvious to those desiring to implement the equations in radiographic applications. Furthermore, we derive an explicit backprojection equation that is related to the forward projection while [12] presents several methods to compute only the geometry.

2 Methods

In this most general implementation of TACT we acquire a set of projection images of an object configured with six fiducial markers that have a fixed and known geometric relationship to each other. The locations of the fiducials in each projection image are then determined. These locations and their correspondence to the fiducials on the object are used to compute the elements of a perspective projection matrix for each projection, which represents the unknown imaging geometry. The perspective projection matrix then is used in a backprojection scheme wherein a set of 2D focal planes through the imaged volume is computed. Finally, the backprojected volumes of each projection are combined to form a single 3D volume.

In this section we describe the algorithm for determining the perspective projection matrix representing the unknown imaging geometry and how this matrix is used in a backprojection scheme. We assume the fiducial locations in each projection image are known and the correspondence between fiducials on the object and projected image are also known.

In a perspective projection situation, the imaged object is positioned between the detector and the x-ray source. The x-ray source is positioned sufficiently far enough above the object so beams pass through the object including the fiducial markers and intersect the detector. The source is also positioned sufficiently close to the object so that perspective distortion is significant in each projection image. Figure 2 shows the perspective projection geometry for a simple configuration of fiducials corresponding to six of the eight corners of a unit cube.

To reconstruct a volume from projections with perspective distortion, we must determine the *location* of the x-ray source. Let $\vec{P} = (P_x, P_y, P_z)$ be the unknown location of the x-ray source, $\vec{X_i'} = (x_i', y_i', z_i')$ be the unknown locations of the fiducials, and $\vec{U_i} = (u_i, v_i)$ be the known (measured) location of the fiducials projected onto the detector. We can write an equation relating the fiducials, projected points, and source location, also known as a forward projection, in parametric form as:

$$\vec{U_i} = \vec{P} + t\left(\vec{X_i'} - \vec{P}\right).$$

Rewriting this equation in terms of the individual components of the vectors,

$$u_i = P_x + t\left(x_i' - P_x\right), \quad v_i = P_y + t\left(y_i' - P_y\right), \quad 0 = P_z + t\left(z_i' - P_z\right) \tag{1}$$

where we have assumed, without loss of generality, that the detector array lies on the $z = 0$ plane. Solving these equations for t, we find

$$t = \frac{P_z}{P_z - z_i'}.$$

In this equation P_z corresponds to the z-component of the x-ray source, which must not be zero or equal to z_i'. Physically, this means the x-ray source cannot lie on the plane of the detector or at the same value of z_i' as any of the fiducials. Substituting this value of t into equation 1 and after some algebraic manipulation, we get

$$u_i = \left(\frac{P_z x_i' - P_x z_i'}{P_z - z_i'}\right), \qquad v_i = \left(\frac{P_z y_i' - P_y z_i'}{P_z - z_i'}\right). \tag{2}$$

The division by $P_z - z_i'$ makes these equations *non-linear* making it difficult to find a solution. Fortunately, we can make these equations linear by representing the quantities in a projective space, also known as *homogeneous coordinates*. In a projective space formulation,

$$\vec{U}_i = \begin{pmatrix} u_i \\ v_i \\ 1 \end{pmatrix}, \quad \vec{X}_i' = \begin{pmatrix} x_i' \\ y_i' \\ z_i' \\ 1 \end{pmatrix}, \quad \text{and } \lambda = P_z - z_i'.$$

Then,

$$\lambda \vec{U}_i = \begin{pmatrix} P_z x_i' - P_x z_i' \\ P_z y_i' - P_y z_i' \\ P_z - z_i' \end{pmatrix} = \mathbf{P}\vec{X}_i', \tag{3}$$

where $\mathbf{P}$ is the forward perspective projection matrix and

$$\mathbf{P} = \begin{pmatrix} P_z & 0 & -P_x & 0 \\ 0 & P_z & -P_y & 0 \\ 0 & 0 & -1 & P_z \end{pmatrix}.$$

With TACT, the x-ray source, object, and detector can be arbitrarily positioned when making a new perspective projection. We can simplify the analysis by noting that moving the object and source relative to a fixed detector can generate any projection. In this case, after applying a rigid body transformation to the object and fiducials in the projective space, we get,

$$\vec{X}_i' = \begin{pmatrix} \mathbf{R} & \vec{T} \\ 0^{\vec{T}} & 1 \end{pmatrix} \vec{X}_i = \overline{\mathbf{R}}\vec{X}_i$$

where $\overline{\mathbf{R}}$ is a 3×3 orthonormal rotation matrix, $\vec{T}$ is a 3×1 translation vector and $\vec{0}$ is a 3×1 null vector. Substituting this representation of $\vec{X}_i'$ into the perspective projection equation (3) we get,

$$\lambda \vec{U}_i = \mathbf{P}\overline{\mathbf{R}}\vec{X}_i = \mathbf{A}\vec{X}_i,$$

where $\mathbf{A}$ is a 3×4 forward perspective projection matrix,

$$A = \begin{pmatrix} a_{11} & a_{12} & a_{13} & a_{14} \\ a_{21} & a_{22} & a_{23} & a_{24} \\ a_{31} & a_{32} & a_{33} & a_{34} \end{pmatrix}$$

A back projection formula can be derived by expanding the above equation, separating terms, and regrouping. We get,

$$\begin{pmatrix} x \\ y \end{pmatrix} = \mathbf{B}^{-1} \left((a_{33}z + 1) \begin{pmatrix} u \\ v \end{pmatrix} - z \begin{pmatrix} a_{13} \\ a_{23} \end{pmatrix} \right),$$

where

$$\mathbf{B} := \begin{pmatrix} a_{11} - a_{31}u & a_{12} - a_{32}u \\ a_{21} - a_{31}v & a_{22} - a_{32}v \end{pmatrix}.$$

Using this equation we can compute all points on a focal plane for a given height (z value) of the plane. Furthermore, the inclusion of the forward projection terms insure the backprojection is performed with the same perspective geometry used to create the projection.

These equations are indirectly implemented in TACT, which is described in the following geometric algorithm.

1. Construct a fiducial model consisting of four coplanar but not collinear points. Frequently, it is convenient for these points to be arranged as square. The plane containing these four points is parallel to the detector array in what we call the *canonical configuration.* Next, two more model points are added such that they are not in the plane containing the the four model points in the canonical configuration. These additional

two points are constrained such that they determine a line that is parallel to the plane containing the square cited above. The model can be rigidly moved from its canonical configuration as long as the fiducial points project onto the detector array and that the projections of the top two points do not coincide.

2. Create as many projections as desired, where each projection results from reorienting the model

3. For each projection

   (a) Identify the projections of the four fiducials that lie on a plane parallel to the detector array when the model is in its canonical configuration.

   (b) Determine the components of a 2D warping transformation that maps the four projected points into the location of the corresponding points in the model in its canonical configuration.

   (c) Apply this warping transformation to all pixels in the projection image, creating a warped projection.

   (d) Identify the additional two points that do not lie in the plane of the other four points in the canonical model and associate these points with their corresponding model points in the warped projection.

   (e) Create two lines that emanate from the two projected points in the warped image and pass through their corresponding fiducial point in the model in its canonical configuration.

   (f) Compute the point of intersection of these two lines. This point represents the location of the x-ray source to create the warped projection from the model in its canonical configuration. This perspective projection is exactly the same as the

perspective projection that created the original projection from the reoriented model.

(g) Use the components of the computed perspective transformation in the back projection equation detailed above and compute focal planes through the imaged volume.

4. Combine the individual volumes computed for each projection using an average, sum, minimum, maximum, median, or any other weighting scheme for generating a single value from multiple estimates [14].

Test Cases

To demonstrate the validity of our method we created a high resolution, simulated, phantom of a patients head within a stereotactic or N-bar frame. These frames are used in a neurosurgical setting to accurately determine a biopsy trajectory for retrieving cranial lesion samples. Typically, neurosurgical scans have a high in-plane resolution and a comparatively low through-plane resolution. Ratios of distances between vertical and diagonal rods in cross-sectional images provides three points that lie on the plane, regardless of whether the plane is exactly parallel to the vertical rods. Because of the frames' localization reliability, we used the frame to assess TACT's reconstruction accuracy, by including two simulated tumors in the head phantom. We compare the tumor locations to the simulated and reconstructed volumes, which is used as an indication of the reconstruction accuracy.

Seven different projections of the simulated volume were made from different projection angles and different x-ray source-to-detector array distances. A tomosynthetic volume was then reconstructed using the algorithm described above by summing individual voxel values computed for each projection. The simulated data set contained 128 different slices, where each slice was 128 X 128 pixels. The volume was isometrically generated at a resolution of

1mm/pixel. Figures 3 a, b, and c respectively show a volume rendering of the simulated data set and two cross-sectional slices depicting two simulated tumors within the brain. These projections were made with the stereotactic frame perpendicular to the detector array, and the x-ray source occupied different locations as shown in Figure 4a and enumerated in 4b.

In these experiments, we removed the error associated with locating the fiducials in each projection image by numerically adding the fiducial locations to the simulated volume and analytically projecting the fiducials onto the detector array. The detector array was square with 512 pixels on a side. The resolution was 1mm/pixel in both orthogonal directions within the array. This configuration insured that all fiducial points were projected onto the detector array, and all could be interactively identified as required by clinical applications of the reconstruction algorithm described above.

The imaging geometry for each projection was then computed using this algorithm, and the projection was back-projected through this geometry creating seven different 3D volumes. The back-projected volumes then were combined into a composite volume by summing the values at each voxel location.

We also reconstructed a tomosynthetic volume from the same seven projections using a standard tomosynthesis reconstruction algorithm (shift and add) that assumes a fixed, parallel projection, imaging geometry. We compared this tomosynthetically created volume to the volume created using the less-constrained TACT reconstruction algorithm.

3 Results

The back-projected volumes for the three projections shown in Figure 5 are displayed in Figure 6. It is clear that the projection image was perspectively back-projected across the reconstruction volume. All seven of the back-projected volumes were combined into a single

composite volume by adding the voxel value for each location within the volume. Figure 7 shows three focal planes reconstructed at different depths within the volume.

We quantified the accuracy of the TACT reconstruction by measuring the ratios of the distance from the center of a vertical rod in the stereotactic frame to the center of a diagonal rod. Figure 8 shows a view of a cross-sectional plane passing through the center of the tumor shown in Figure 3c and the stereotactic frame. Each rod in the figure is assigned a number from 1 to 7, and the coordinates of the rod center are also shown. The table in Figure 8 shows the distance between adjacent frame rods as the number of pixels between rod centers.

The ratio of the distance between rod 1 and 2 to rod 2 and 3 is $\frac{130}{50} = 2.6$. Likewise, the ratio of the distance between rods 3, 4, and 5 is: $\frac{133}{48} = 2.77$, and the ratio of distances between rods 5, 6, and 7 is: $\frac{134}{47} = 2.85$. These values are shown in Table 1 along with the corresponding measures for the same slice in the reconstructed volume. We made similar tables for a slice passing through the tumor located at the top of the head, where the results are shown in Table 2.

Standard Tomosynthetic Reconstruction Algorithm

Figure 9 shows three slices of the reconstructed volume generated with a standard tomosynthesis reconstruction algorithm. The blurring in this figure is so severe that it made tube center identification impossible and therefore this reconstructed volume was not quantified.

4 Discussion

With only seven projection x-ray images of the simulated head phantom, TACT successfully reconstructed a volume that clearly depicts both the lower and upper tumors as shown in Figure 7 a and b. Furthermore, using the simulated stereotactic frame as a basis for objective measurement, we found that the geometry within the TACT reconstruction is preserved.

The reconstructed volume contains some blurring, but it is significantly less than that of the control produced using a standard tomosynthesis reconstruction method. The reason TACT provides a clearer reconstruction is that we "undo" the perspective distortion introduced when acquiring projection images. The projections simulated in this investigation had a significant amount of perspective distortion caused by positioning the x-ray source relatively close to the object. In fact, the source position varied from 20 cm away from the center of the object to 47.5 cm while the distance from the object center to the detector array remained constant at 10 cm. Removing the perspective, preserves the geometry of the object and allows elements to be scaled correctly thus reinforcing each other through more precise superposition.

The geometric interpretation requires determining the intersection of two 3D lines. In general these lines may not intersect so we compute the midpoint of a line that is mutually perpendicular to both lines. That is, the line segment representing the minimum distance between the two lines. The computed point then corresponds to the location of the source to generate the warped projection image.

All seven of the back-projected volumes were combined into a single composite volume by adding the voxel value for each location within the volume. Figure 7 shows three focal planes reconstructed at different depths within the volume. Although we have shown volume rendered results, this may not be the best way to visualize tomosynthetic reconstructions. Figure 6 clearly shows blurring caused by the stereotactic frame. The reconstructed values of the rods closely correspond to those associated with the simulated head. Therefore, we could not find a suitable gray value mapping that rendered the frame transparent while making the head opaque. We found sequentially scanning through the slices a more useful visualization technique for this data set.

5 Summary and Conclusions

This paper provides a rigorous mathematical description of TACT. A schematic geometrical simulation was used to produce a relatively unconstrained representative projection model. Results obtained from this model were used to compare reconstruction accuracy produced using the TACT reconstruction scheme with that obtainable from conventional (uncorrected) tomosynthesis. The simulation results confirm the mathematical theory underlying this paper by demonstrating that TACT reconstructions were more accurate than those produced tomosynthetically. Alternatively stated, conventional tomosynthesis produces scaling errors that degrade reconstruction accuracy compared to that obtained using TACT unless the underlying projection geometry is truly affine or some sort of additional projection or magnification correction scheme is applied.

References

1. R. L. Webber, R. A. Horton, D. A. Tyndall, J. B. Ludlow, Tuned-aperture computed tomography (TACT). Theory and application for three-dimensional dento-alveolar imaging, Dentomaxillofacial Radiology 26 (1997) 53–62.
2. D. G. Grant, Tomosynthesis: A three-dimensional radiographic imaging technique, IEEE Transactions of Biomedical Engineering 19 (1972) 20–28.
3. Z. Kolitsi, G. Panayiotakis, V. Anastassopoulos, A. Scodras, N. Pallikarakis, A multiple projection method for digital tomosynthesis, Medical Physics 19(4) (1992) 1045–1050.
4. G. Messaris, Z. Kolitsi, C. Badea, N. Pallikarakis, Three-dimensional localisation based on projectional and tomographic image correlation: an application for digital tomosynthesis, Medical Engineering and Physics 21 (1999) 101–109.
5. C. E. Metz, L. E.Fencil, Determination of three-dimensional structure in biplane radiography, without prior knowledge of the relationship between the two views, Medical Physics 16 (1989) 45 – 51.
6. S. Li, and G. T. Y. Chen, C. A. Pelizzari, C. Reft, J. C. Roeske, Y. Lu, A new source localization algorithm with no requirements of one-to-one source correspondence between biplane radiographs, Medical

Physics 23(6) (1996) 921 – 927.

7. G. M. Stevens, R. Sanders, N. J. Pelc, Alignment of a volumetric tomography system, Medical Physics 28(7) (2001) 1472 - 1481.
8. A. C. Kak, M. Slaney, Principles of Computerized Tomographic Imaging, IEEE Press, New York, NY, 1988.
9. L. T. Niklason, B. T. Christian, L. E. Niklason, D.B. Kopans, D.E. Castleberry, B.H. Opsahl-ong, C.E. Lanberg, P.J. Slantz, A.A. Giardino, R. Moore, D. Albagli, M.C. DeJule, P.F. Fitzgerald,D.F. Fobare, B.W. GiamBattista, R.F. Kwasnick, J. Liu, S.J. Libowski, G.E. Possin, J.F. Richotte, C.Y. Wei, R.F. Wirth, Digital Tomosynthesis in Breast Imaging, Radiology, 205, 399–405, 1997
10. L. T. Niklason, et.al., Tomosynthesis System for Breast Imaging, U.S. Patent # 5,872,828 (1999)
11. S. B. Robinson, P. F. Hemler, R. L. Webber, A geometric problem in medical imaging, in: Proceedings of the SPIE Conference on Mathematical Modeling, Estimation, and Imaging, SPIE, San Diego, CA, 2000.
12. O. Faugeras, Three-Dimensional Computer Vision, A Geometric Viewpoint, The MIT Press, Cambridge, MA, 1993.
13. R. M. Haralick, Using Perspective Transformations in Scene Analysis. Computer Graphics and Image Processing 13, 191-221 (1980).
14. R. L. Webber, P. F. Hemler, J. Lavery, Objective evaluation of linear and nonlinear tomosynthetic reconstruction algorithms, in: Processings of the SPIE Conference on Medical Imaging 2000, vol 3981 Feb. 16-17, San Diego

rod	rod	distance	ratio
1	2	130	$\frac{130}{50} = 2.6$
2	3	50	
3	4	133	$\frac{133}{48} = 2.77$
4	5	48	
5	6	134	$\frac{134}{24} = 2.85$
6	7	24	

a

rod	rod	distance	ratio
1	2	66	$\frac{66}{24} = 2.75$
2	3	24	
3	4	76	$\frac{67}{23} = 2.91$
4	5	23	
5	6	66	$\frac{66}{24} = 2.75$
6	7	24	

b

Table 1. Pixel distances between different rods of the stereotactic or N-bar frame for (a) the simulated volume, (b) the TACT reconstructed volume.

rod	rod	distance	ratio
1	2	37	$\frac{37}{53} = 0.70$
2	3	53	
3	4	37	$\frac{37}{53} = 0.70$
4	5	53	
5	6	37	$\frac{37}{53} = 0.70$
6	7	53	

a

rod	rod	distance	ratio
1	2	74	$\frac{74}{105} = 0.70$
2	3	105	
3	4	73	$\frac{73}{108} = 0.68$
4	5	108	
5	6	75	$\frac{74}{104} = 0.70$
6	7	104	

b

Table 2. Pixel distances between different rods in the stereotactic or N-bar frame for a slice passing through the tumor near the top of the head. The table on the left (a) indicates the pixel distances and ratios of the simulated volume, while the table on the right (b) shows pixel distances for the reconstructed volume.

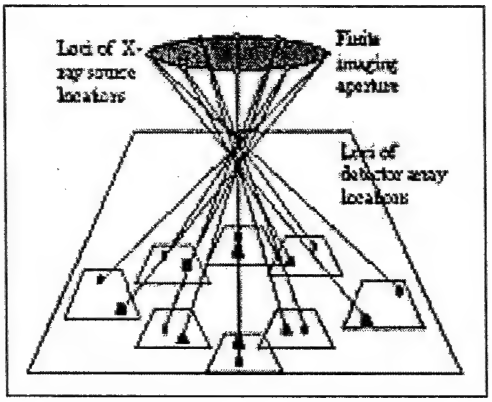

a

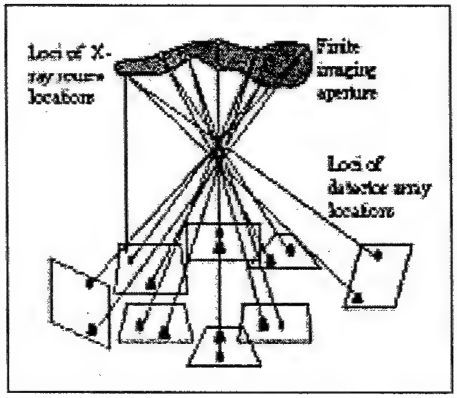

b

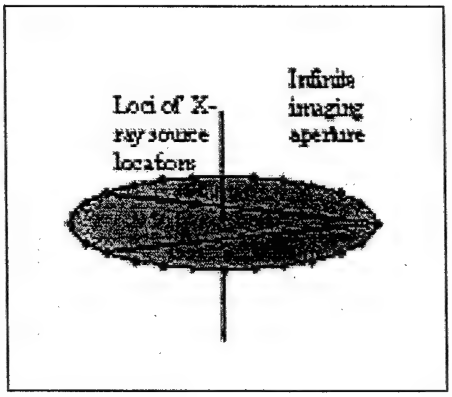

c

Fig. 1. Imaging geometry for a) Circular Tomosynthesis, b) TACT, and c) CT. Circular tomosynthesis and TACT have approximately the same imaging aperature, while CT has an infinite aperature.

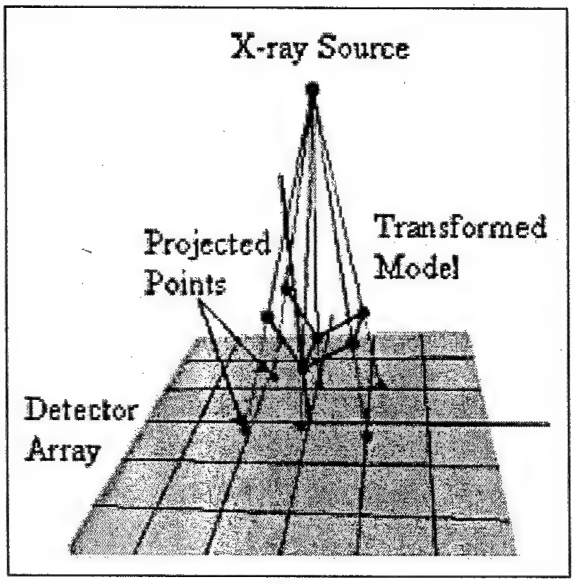

Fig. 2. Perspective projection imaging geometry for a simple cube model.

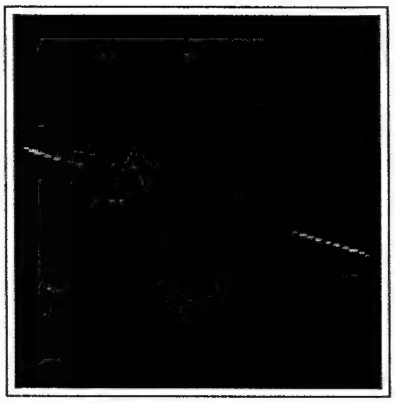

a

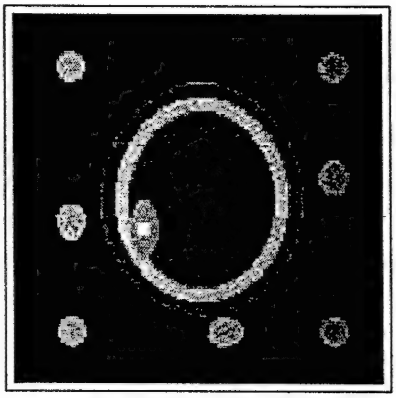

b

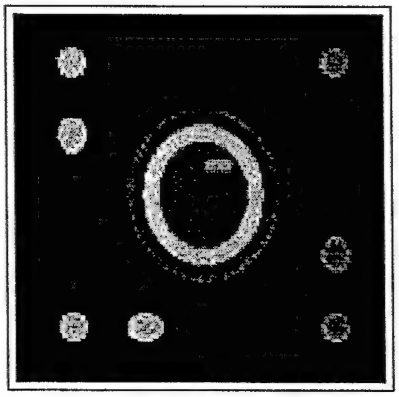

c

Fig. 3. Volume rendering (a) and cross-sectional images (b and c) of a simulated head including two tumors. The simulated head phantom is located inside a simulated stereotactic or N-bar frame, which is used to demonstrate the accuracy of our reconstructed volume.

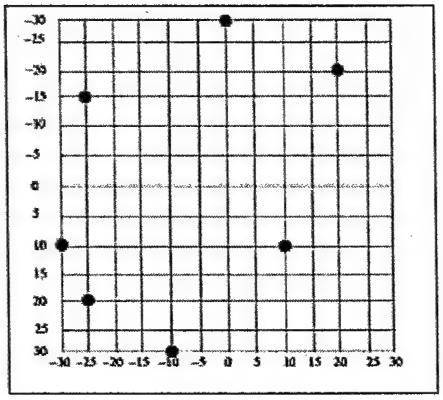

a

projection	Rx	Ry	distance
1	−30	10	310
2	−25	20	240
3	−10	30	325
4	10	10	475
5	20	−20	200
6	0	−30	400
7	−25	−15	300

b

Fig. 4. Angular displacements from perpendicular to the detector array of (a) the x-ray source and (b) tabulation for each of the seven projections. Both axes of the grid are in degrees measured from the z-axis. Rx corresponds to a rotation about the x-axis and is represented by the vertical axis. Ry corresponds to a rotation about the y-axis and is represented by the horizontal axis. The distance in the table is measured in mm from the center of the imaged object to the x-ray source.

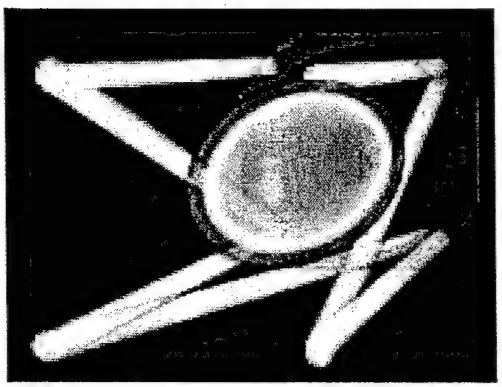

a

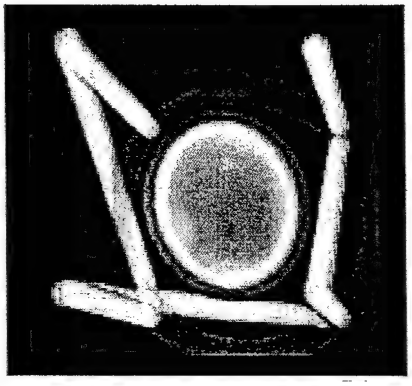

b

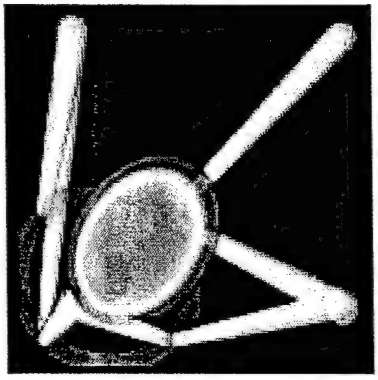

c

Fig. 5. Three of the seven projections of the simulated head phantom for a) projection 3, b) projection 4, c) projection 5.

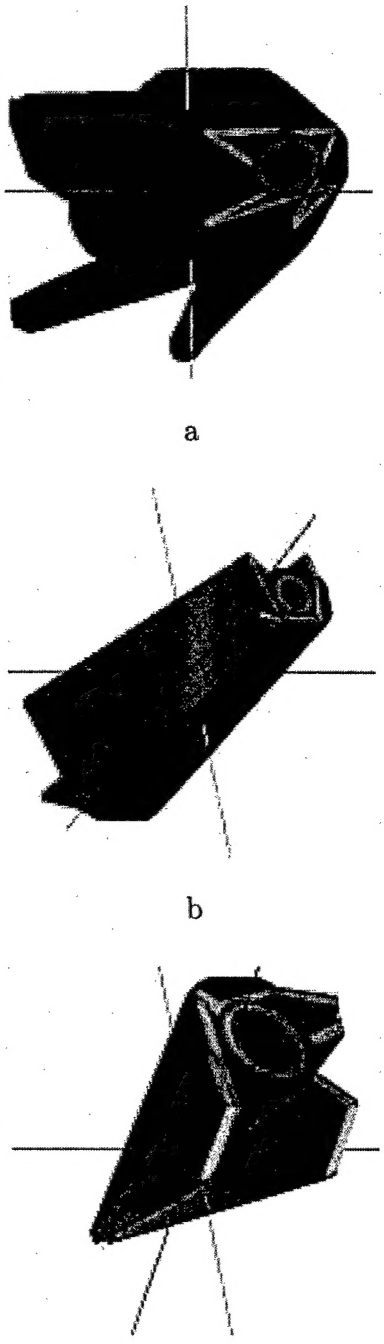

Fig. 6. Three of the seven back-projected volumes of the simulated head phantom, where the x-ray source was rotated a) projection 3, b) projection 4, c) projection 5. This figure is included to demonstrate the nature of perspective backprojection algorithm.

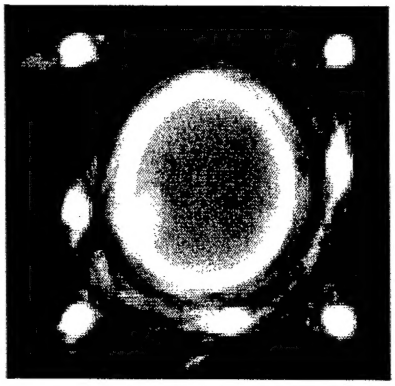

a

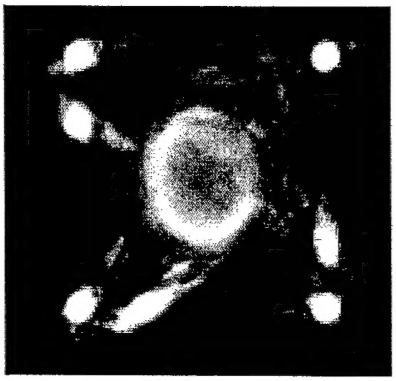

b

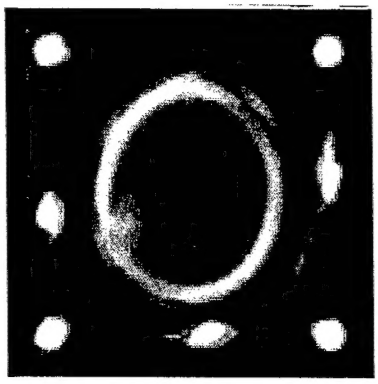

c

Fig. 7. Three focal planes at different depths throughout the reconstructed volume. a) is a focal plane through the tumor in the lower left of the image, b) is a focal plane through the tumor at the top of the head, and c) is the same focal plane as in a, but with the contrast adjusted to highlight the positions of the stereotactic frame and the bright spot in the center of the tumor.

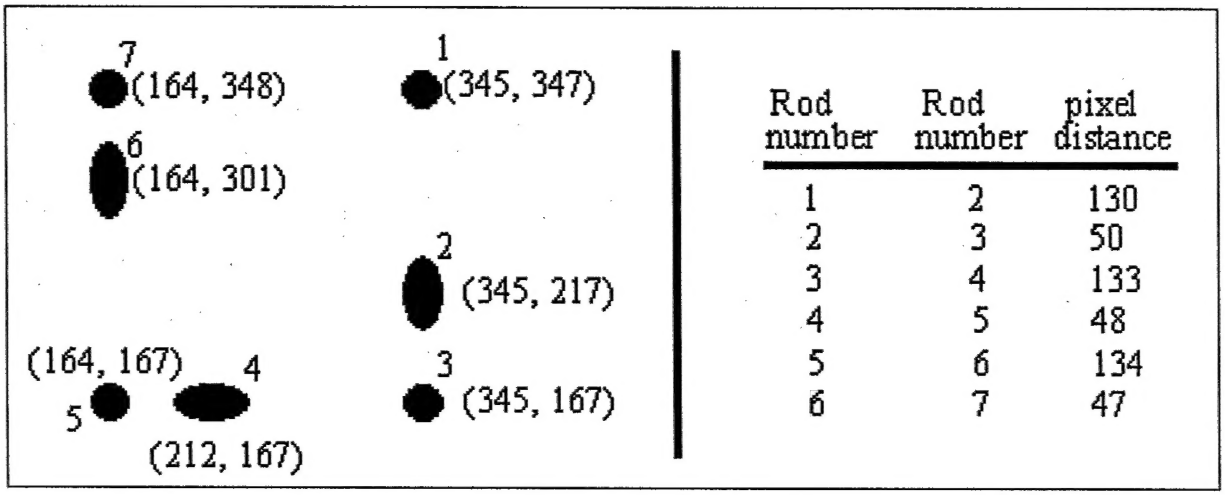

Rod number	Rod number	pixel distance
1	2	130
2	3	50
3	4	133
4	5	48
5	6	134
6	7	47

Fig. 8. An overview of the rod locations in the simulated volume and a table of distances in pixels between adjacent rod centers.

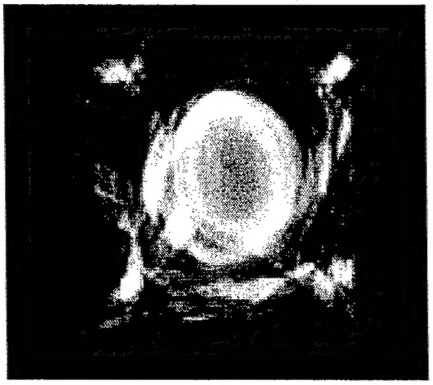

a

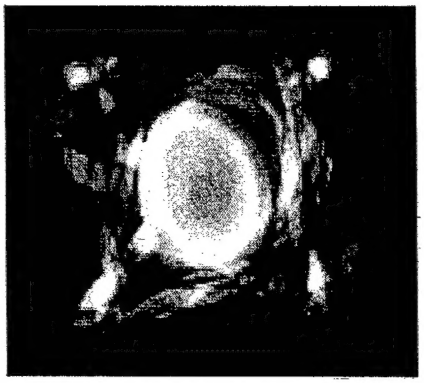

b

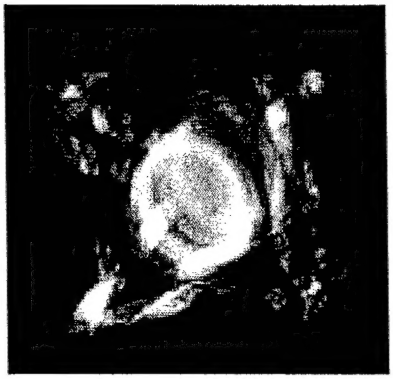

c

Fig. 9. Focal planes through the volume of a tomosynthetic volume reconstructed using a standard tomosynthesis algorithm, where a) is a slice near the lower tumor, b) is a slice through the center, and c) is a slice through the tumor in the top of the head.